Impacts of Synoptic-Scale Dynamics on Clouds and Radiation in High Southern Latitudes

Tyler Barone[1,*], Minghui Diao[1,#], Yang Shi[2,**], Xi Zhao[2,***], Xiaohong Liu[2], Israel Silber[3,****]

1 Department of Meteorology and Climate Science, San Jose State University, San Jose CA, 95192.

2 Department of Atmospheric Sciences, Texas A&M University, College Station TX, 77843.

3Department of Meteorology and Atmospheric Science, Pennsylvania State University, University Park, PA, 16802.

*Current affiliation: Department of Atmospheric Sciences, Texas A&M University, College Station TX, 77843.

**Current affiliation: Department of Civil and Environmental Engineering, Massachusetts Institute of Technology, Cambridge, MA, 02139.

***Current affiliation: Institute of Surface-Earth System Science, School of Earth System Science, Tianjin University, Tianjin, China.

****Current affiliation: Atmospheric, Climate, and Earth Sciences Division, Pacific Northwest National Laboratory, Richland, WA, USA, 99352

#Corresponding author:

Minghui Diao, Ph.D., Associate Professor

Email: Minghui.diao@sjsu.edu

Key Points

- Extratropical cyclone compositing shows more asymmetric cloud properties in eastern and western sectors at McMurdo than Macquarie Island

- Simulated IWP is too low at both sectors and both sites; LWP is too high (low) at Macquarie (McMurdo)

- Model radiation biases are affected by both cloud properties and synoptic dynamics (e.g., extratropical cyclones)

Keywords: Southern Ocean; Clouds and Radiation; Synoptic dynamics; Extratropical cyclones; DOE MICRE and AWARE campaigns; CAM6 and EAMv1 climate models.

Abstract

High-latitudinal mixed-phase clouds significantly affect Earth's radiative balance. Observations of cloud and radiative properties from two field campaigns in the Southern Ocean and Antarctica were compared with two global climate model simulations. A cyclone compositing method was used to quantify "dynamics-cloud-radiation" relationships relative to the extratropical cyclone centers. Observations show larger asymmetry in cloud and radiative properties between western and eastern sectors at McMurdo compared with Macquarie Island. Most observed quantities at McMurdo are higher in the western (i.e., post-frontal) than the eastern (frontal) sector, including cloud fraction, liquid water path (LWP), net surface shortwave and longwave radiation (SW and LW), except for ice water path (IWP) being higher in the eastern sector.

The two models were found to overestimate cloud fraction and LWP at Macquarie Island but underestimate them at McMurdo Station. IWP is consistently underestimated at both locations, both sectors, and in all seasons. Biases of cloud fraction, LWP, and IWP are negatively correlated with SW biases and positively correlated with LW biases. The persistent negative IWP biases may have become one of the leading causes of radiative biases over the high southern latitudes, after correcting the underestimation of supercooled liquid water in the older model versions. By examining multi-scale factors from cloud microphysics to synoptic dynamics, this work will help increase the fidelity of climate simulations in this remote region.

Plain Language Summary

The efficacy of climate prediction is largely dependent on accurately estimating Earth's energy budget in global climate models. The Southern Ocean region has a distinct history of showing large biases in energy budget within global climate models. This region also shows complex interactions between large-scale dynamical conditions (e.g., low-pressure systems) and microscale processes (e.g., cloud properties). This work used two field deployments at Macquarie Island, Southern Ocean and McMurdo Station, Antarctica to understand these interactions. Observations were obtained from year-long measurements by ground-based instruments, which were further compared with two global climate models. The two models were found to have errors representing cloud properties at Macquarie Island (e.g., too much liquid and too little ice) and McMurdo Station (e.g., too little ice and liquid), as well as errors representing net surface longwave (terrestrial) radiation and shortwave (solar) radiation. The combination of the insufficient amounts of cloud ice and liquid in the models at McMurdo, Antarctica may be the main cause of too much solar radiation absorbed by Earth's surface over that region, which also have implications for polar ice melting and ocean circulation in that remote region.

1. Introduction

Clouds are significant modulators of the Earth's energy balance, since they can affect the absorbed shortwave radiation (ASR) and outgoing longwave radiation (OLR) (Liou, 1992). Clouds over oceans have large influences on the regional radiative budget due to the sharp contrast in albedo between the highly reflective cloud layers and the dark ocean surface (e.g., Klein & Hartmann, 1993; Bender et al., 2011; Raschke et al., 2016). As discussed in Trenberth and Fasullo (2010), model biases of cloud cover and radiation in the ocean-dominated Southern Hemisphere can lead to errors in poleward energy transport and development of baroclinic eddies and storm tracks. The future projection is also particularly sensitive to simulated cloud cover over the Southern Ocean, since a strong relationship between projected cloud cover changes and present-day simulated cloud cover errors were found over this region in that study. The Southern Ocean circulation further affects sea level rise and ice melting in the southern high latitudes (Holland et al., 2010; Bouttes et al., 2012). This is also a region that connects deep ocean water with ocean upwelling and surface air (Marshall and Speer, 2012). The prediction of these interactive processes among atmosphere, ocean, ice, and land in a future climate relies on accurate representations of the surface radiation budget (e.g., Essery et al., 2003; Gleckler, 2005).

Global climate models (GCMs) have shown large sensitivities in their prediction of the radiation budget of Earth's climate system due to the variations in the representations of Southern Ocean clouds (e.g., Klein et al., 2017; McCoy et al., 2014a, 2014b, 2015, 2016, 2019; Tan et al., 2016; Terai et al., 2016; Zelinka et al., 2020). A metric used by climate models to quantify sensitivities of Earth's climate to the emissions of anthropogenic greenhouse gases is the equilibrium climate sensitivity (ECS). The ECS value represents the magnitude of air temperature rise at the Earth's surface after the climate system reaches a new equilibrium due to an instantaneous doubling of carbon dioxide concentrations in the atmosphere. Several studies have shown extratropical low-level clouds play a significant role in contributing to the large variations of ECS among numerous climate models (Collins et al., 2013; Flynn & Mauritsen, 2020; Zelinka et al., 2020). In fact, the Intergovernmental Panel on Climate Change (IPCC) reported a large variation of ECS by various GCMs, which is likely in the range of 1.5°C to 4.5°C in the IPCC 5th assessment report (AR5) (IPCC AR5, 2013) and likely in the range of 2.5°C to 4.0°C in IPCC 6th assessment report (AR6) (IPCC AR6, 2023). Thus, in order to reduce uncertainties of future climate predictions, improved understanding of Southern Ocean cloud properties based on observational analysis is crucial for model development.

Two specific properties of Southern Ocean clouds are the main foci of this study – the spatial extent of clouds (i.e., represented by cloud fraction) and the cloud thermodynamic phase (reflected by the amount of liquid and ice hydrometeors). Several previous studies have shown large sensitivities of ECS values to the representations of mixed-phase clouds in the mid- to high latitudes, especially to the treatment of cloud thermodynamic phases in the GCMs (e.g., Tsushima et al. 2006; Tan et al. 2016; Bjordal et al. 2020). Cloud thermodynamic phases are highly sensitive to temperature perturbations. A negative cloud feedback would occur when the ice phase transitions into liquid phase (e.g., Mitchell et al., 1989; Ceppi et al., 2016). That is because liquid phase contains high concentrations of liquid droplets, which produce higher albedo and can reflect more solar radiation compared with ice phase, and therefore the reflected solar radiation increases when ice transitions to liquid phase. In addition, a transition from ice to liquid has a large impact on cloud top cooling rates in the LW and can also increase surface temperature by increasing surface LW radiation. Such surface warming effect via intensified LW radiation is typically a smaller effect than the enhanced SW cooling effect for low clouds. If the total water content of clouds remains the same, a higher amount of ice hydrometeors initially existing in clouds would allow a larger magnitude of phase change from ice to liquid, which can partly buffer the global warming effect induced by greenhouse gases. Therefore, the partitioning between liquid and ice phases, which can be partly represented by LWP and IWP, can directly affect the potential change from ice to liquid phase in clouds as temperature increases, which further leads to significant impacts on climate sensitivities due to warming as discussed in previous studies (e.g., Tsushima et al. 2006; Tan et al. 2016; Bjordal et al. 2020). The extensive cloud coverage over the high southern latitudes and the large variability in their microphysical and macrophysical properties have been previously reported in observational studies (e.g., D'Alessandro et al., 2019; Yang et al., 2021; Yip et al., 2021; Maciel et al., 2024; D'Alessandro et al., 2023; Desai et al., 2023), which illustrate the inherent complexity of representing these properties in GCMs. These former studies have examined multiple factors controlling mixed-phase cloud properties, including thermodynamic conditions (i.e., temperature and relative humidity), dynamic conditions (e.g., vertical velocity), and aerosol indirect effects. One particular factor that requires more detailed investigation is the influence of synoptic dynamical conditions on cloud macrophysical and microphysical properties.

Extratropical cyclone activity over the Southern Ocean region has been previously documented to affect concurrent cloud and radiation properties, such as cloud type, cover, thickness, cloud-top height, LWP, and the radiation budget at the top of the atmosphere (e.g., Bodas-Salcedo et al., 2012, 2014, 2016, 2019; Williams et al. 2013; Kelleher & Grise, 2019; Montoya Duque et. al., 2022). Previous studies developed various methods to define dynamical regimes surrounding extratropical cyclones, known as the cyclone compositing methods, in order to assess the cloud properties in different quadrants relative to extratropical cyclone or anticyclone centers (Lau & Crane 1995, 1997; Naud et al., 2006, 2010; Field & Wood, 2007; Posselt et al., 2008; Field et al., 2011). Distinctive dynamical conditions were found in two sectors – the warm sector that is dynamically active in the frontal region, and the cold sector that is dynamically suppressed in the post-frontal region. Thus, evaluation studies of GCMs frequently targeted the "dynamics-cloud" relationship, which originates from the parameterizations of microscale cloud properties in response to different thermodynamic and dynamic conditions. Using the cyclone compositing methods, previous work showed that cloud and radiation biases in model simulations and reanalysis data are larger in the cold sectors of the extratropical cyclones over the Southern Ocean (Bodas-Salcedo et al. 2012, 2014; Williams et al. 2013; Naud et al. 2014).

For the evaluation of GCMs against observations, many previous studies on Southern Ocean clouds and dynamics utilized spaceborne remote sensing observations to compare with GCM simulations, such as using the Cloud-Aerosol Lidar and Infrared Pathfinder Satellite Observations (CALIPSO) data to assess simulated cloud properties including cloud fraction (e.g., Bodas-Salcedo et al., 2012, 2014; Zhang et al., 2021), optical depth (Terai et al., 2016), and thermodynamic phase (Kay et al., 2016). Other studies used the Clouds and the Earth's Radiant Energy System (CERES) satellite-based observations of radiative forcings to assess shortwave cloud forcing at the top of the atmosphere (Ceppi et al., 2012; Hwang et al., 2013), and SW and LW radiation at the top of the atmosphere (Trenberth & Fasullo, 2010). More recent studies also evaluated GCMs from the Coupled Model Intercomparison Project 6 (CMIP6) against satellite-based observations such as CALIPSO, CERES, Moderate Resolution Imaging Spectroradiometer

(MODIS), and International Satellite Cloud Climatology Project (ISCCP) (e.g., Schuddeboom & McDonald, 2021; Cesana et al., 2022; Zhao et al., 2022). On the other hand, with increasing availability of flight campaigns over the high southern latitudes, other studies also used airborne in-situ, ship-based, and ground-based remote sensing observations to evaluate simulated cloud microphysical properties in various GCMs (e.g., D'Alessandro et al., 2019; Gettelman et al., 2020; Yang et al., 2021; Yip et al., 2021; Desai et al., 2023). When validating three satellite-based cloud phase products against in-situ airborne observations, CALIPSO, CloudSat, and DARDAR (raDAR/liDAR) data do not agree with each other and show different biases of cloud phase partitioning at various latitudes compared with in-situ observations (Wang et al., 2024). Because of this, more studies using ground-based or airborne observations are needed to examine the "dynamics-cloud" relationship as an independent evaluation that can complement the satellite-based model evaluation.

In this work, unique observational datasets are obtained from ground-based remote sensing measurements at two locations – Macquarie Island and McMurdo Station, Antarctica. These two stations are located at the north and south side of the Southern Hemisphere storm track, respectively (Taljaard, 1972; Hoskins & Hodges, 2005; Chapman et al., 2015). Two field campaigns from these locations provide year-long measurements on cloud fraction, LWP, and surface SW and LW radiation. These ground-based measurements have unique advantages compared with spaceborne observations that retrieve radiation at the top of the atmosphere. Satellite observations commonly have lidar signal attenuation issues when encountering opaque liquid-containing clouds and radar blind zone at heights below 1 km above the surface, where low-level clouds are ubiquitously seen over this region (Cesana & Chepfer, 2013; Silber et al., 2018; Liu, 2022). In addition, the ground-based measurements of cloud fraction, LWP, and net surface radiation are analyzed at hourly basis in this work, which is a higher frequency than the daily or monthly averages previously used in analysis of dynamics-cloud relationships in this region (e.g., Govekar et al., 2011, 2014; Bodas-Salcedo et al., 2012, 2014, 2016; Williams et al., 2013; Kelleher & Grise, 2019). These ground-based observations are uniquely poised to answer a range of science questions: (i) What are the synoptic-scale dynamical influences on cloud and radiative properties at Macquarie Island and McMurdo Station based on observations and what are the differences between the two locations? (ii) What are the model biases in dynamics-cloud-radiation relationships as well as their individual characteristics? And (iii) How do various controlling factors contribute to model biases of net surface radiation? In Section 2, observation datasets and experimental setup of simulations from two GCMs in the CMIP6 are described. Section 3 examines cloud and radiative properties as well as their relationships with extratropical cyclones over the Southern Ocean using a cyclone compositing method. Lastly, discussions of the main conclusions and implications for future model development are given in Section 4.

2. Observations, reanalysis data, and climate model simulations

2.1 Ground-based observations and reanalysis data over the Southern Ocean and Antarctica

The Department of Energy (DOE) Atmospheric Radiation Measurement (ARM) Macquarie Island Cloud and Radiation Experiment (MICRE) campaign provided an extensive ground-based observational dataset during the time period of March 1, 2016, to March 31, 2018 (Marchand et al., 2020; McFarquhar et al., 2021). The MICRE campaign was supported by the DOE ARM program, the Australian Antarctic Division (AAD), and the Australian Bureau of Meteorology

(BoM), and was located on Macquarie Island at 54.5°S, 158.9°E. Climatologies of weather conditions at MICRE have been previously investigated (Hande et al., 2012; Wang et al., 2015). Surface observations from the MICRE campaign have been used in previous studies with a special focus on seasonal variations of aerosols (Humphries et al., 2023), cloud and precipitation (Tansey et al., 2022, 2023; Stanford et al., 2023) and radiation (Hinkelman & Marchand, 2020). A suite of instruments was deployed in the MICRE campaign, which was listed in the overview article of McFarquhar et al. (2021) in their Table S1. The main instruments included the DOE sky radiation radiometers (SKYRAD), ground radiation radiometers (GNDRAD), ceilometer, microwave radiometer, sun photometer, and a multi-filter rotating shadowband radiometer (MFRSR). A value-added product (VAP) named as Cloud Optical Properties from the Multi-filter Shadowband Radiometer (MFRSRCLDOD; Turner et al., 2021) provides observed cloud properties (e.g., LWP and cloud fraction) derived from a combination of instruments, such as MFRSR, microwave radiometer, GNDRAD, SKYRAD, and ceilometer. The cloud fraction provided in this product represents cloud fractional sky cover over a hemispheric dome. IWP was derived from the 94 GHz cloud radar (named as BASTA) observations (Delanoë et al., 2016; Mace and Protat, 2018) by estimating and vertically integrating ice water content (IWC) (Hogan et al. 2006). Another VAP product named as Radiative Flux Analysis (RADFLUX1LONG; Riihimaki et al., 2019) compiled radiative measurements from GNDRAD, SKYRAD, and the MFRSR. This VAP provides estimates of surface radiation flux, including longwave broadband total downwelling and upwelling irradiances, shortwave broadband diffuse downwelling irradiances, shortwave broadband direct normal irradiances, and shortwave broadband total downwelling irradiances. The quality control test and procedure of radiation measurements were described in Long and Shi (2006, 2008).

The ARM West Antarctic Radiation Experiment (AWARE) was co-funded by the US DOE and US National Science Foundation (NSF) (Lubin et al., 2020). The second ARM mobile facility (AMF2) was deployed from December 2015 to January 2017 at the US McMurdo Research Station located in Ross Island, Antarctica, at 77.85°S, 166.66°E. An ARM best estimate (ARMBE) data product (awrarmbecldradM1.c1) provides the total cloud fraction measurements. This cloud fraction product was derived using measurements from cloud radar and micropulse lidar (Xie et al., 2010). Solar and infrared radiation observations were used to estimate hourly mean surface longwave and shortwave irradiances (Silber et al., 2019a). Downwelling and upwelling radiation measurement uncertainty follows the Solar Infrared Radiation Station (SIRS) handbook, documented in Andreas et al. (2018). We used LWP from the MWR and G-band (183 GHz) Vapor Radiometer profiler (GVRP) when available. Note that the LWP data were missing for the entire month of January in 2017 in AWARE since during that period, the MWR used to retrieve the LWP was deployed in the secondary AWARE site over the West Antarctic Ice Sheet (WAIS). The Ka-band ARM Zenith Radar (KAZR) reflectivity and (linearly interpolated) sounding temperature measurements were used to derive IWC based on the equations for IWC retrieval (Hogan et al., 2006). Values of IWC were then vertically integrated to derive IWP. Cloud phase observations were derived from observations of KAZR (Widener et al., 2012) and High Spectral Resolution Lidar (HSRL; Eloranta, 2006) based on the method from Silber et al. (2018). Radiosondes were released twice daily at AWARE, providing temperature and water vapor partial pressure profiles. These data can be used to derive relative humidity with respect to ice (RHice) and relative humidity with respect to liquid (RHliq) based on the equations of saturation vapor pressure with respect to ice and liquid in Murphy and Koop (2005), respectively.

The National Centers for Environmental Prediction (NCEP) – National Center for Atmospheric Research (NCAR) reanalysis data document the 6-hourly sea level pressure variable, with a spatial resolution of 2.5° × 2.5° globally (Kalnay et al., 1996). The sea level pressure distributions and synoptic conditions were analyzed using the NCEP reanalysis data in 2016 and 2017, specifically targeting the ground station locations of McMurdo Station and Macquarie Island, respectively.

2.2 Climate model simulations

Simulations of two GCMs were conducted, and the model output was used for comparisons with observations from the MICRE and AWARE campaigns. The first global climate model is the Community Earth System Model version 2 (CESM2) (Danabasoglu et al., 2020). Its atmosphere component is called Community Atmosphere Model version 6 (CAM6). The CESM2/CAM6 model is primarily developed by NCAR, and its main configuration is described as follows. The Cloud Layers Unified by Binormals (CLUBB) scheme (Larson et al., 2002; Golaz et al., 2002a, 2002b; Bogenschutz et al., 2013) is coupled with the Morrison-Gettelman double-moment microphysics scheme (MG2) (Gettelman & Morrison, 2015; Gettelman et al., 2015), which contains four classes of hydrometeors: liquid droplets, ice particles, snow, and rain. A four-mode aerosol model (MAM4) based on Liu et al. (2016) is also coupled with MG2. Radiation is calculated in the CAM6 simulation by the Rapid Radiative Transfer Model for General Circulation Models (RRTMG) (Iacono et al., 2000).

This work also evaluates simulations from the DOE Energy Exascale Earth System Model version 1 (E3SM1) (Golaz et al., 2019), specifically its atmosphere component – E3SM Atmosphere Model version 1 (EAMv1) (Rasch et al., 2019). Similar to CAM6, EAMv1 incorporates the coupled MG2 and CLUBB for cloud parameterizations, and its radiation scheme uses RRTMG. The CAM6 simulations use the default 32 sigma hybrid pressure layers and a horizontal grid size of 0.5° latitude by 0.63° longitude. The vertical resolution of EAMv1 is the default 72 sigma hybrid pressure layers, and its horizontal resolution is approximately 1° latitude by 1° longitude. As for the similarities and differences between the two climate models, the horizontal resolution for CAM6 and EAMv1 are both around 1 degree but CAM6 uses a finite volume dynamical core, while EAMv1 uses a spectral element core. In addition, the vertical resolution of EAMv1 (i.e., 72 vertical layers) is finer compared with CAM6 with 32 layers. The two models share the same physical parameterizations for deep convection, shallow convection, cloud macrophysics, and cloud microphysics, but different tuning parameters are applied. A major difference is that the Wegener-Bergeron-Findeisen (WBF) process is scaled down by a factor of 10 in EAMv1 compared to CAM6.

For both CAM6 and EAMv1 simulations, their temperature and horizontal wind fields were nudged towards the MERRA-2 reanalysis data, in order to focus our analyses on clouds and radiation. The nudged simulations were run over the entire period of MICRE and AWARE campaigns separately, with a 6-month spin-up time in each simulation. The nudging methodology is consistent with previous studies that compare GCM output with shipborne (Desai et al., 2023), ground-based (Yip et al., 2021) and airborne (Yang et al., 2021; Zhao et al., 2023) observations. For the evaluation of cloud and radiative properties, the model output was saved as a single-column output, collocated with either McMurdo Station or Macquarie Island. That is, the closest grid box with respect to each station location was selected. Since both sites are close to the ocean, the model grids are over a mixture of land and ocean for both EAMv1 and CAM6. Another type of model output was saved over the entire region of Southern Ocean for the purpose of evaluating simulated synoptic conditions against the reanalysis data, specifically for sea level pressure distributions and low-pressure system locations. The model output of cloud properties – cloud fraction, LWP and IWP – were at 30-minute frequency, while the model output of radiative properties in SW and LW were saved at 1-hour frequency.

Several variables were further derived to facilitate comparisons between model simulations and observations. For the analysis of radiative properties in observations and simulations, net surface radiation is defined as the downwelling component minus the upwelling component for both SW and LW radiation (i.e., positive net values indicate net gain of energy). To reduce the radiative biases in models caused by discrepancies of surface albedo, we replaced the simulated albedo with the observed albedo for SW radiation, and re-calculated the upwelling SW radiation component in CAM6 and EAMv1 as shown in Equation (1), where $SW_{up,obs}/SW_{down,obs}$ equals the observed surface albedo:

$$SW_{up,model} = SW_{down,model} \times \frac{SW_{up,obs}}{SW_{down,obs}} \quad (1)$$

For comparisons of cloud properties, a threshold of cloud fraction > 10^{-4} was applied to model output to denote in-cloud conditions, following the threshold used in previous studies (D'Alessandro et al., 2019; Yip et al., 2021; Desai et al., 2023). Furthermore, a minimum threshold of cloud water content (i.e., the sum of ice and liquid water content) of 10^{-7} g m^{-3} was used as an additional necessary criterion to define the in-cloud condition. A similar threshold was also used in previous evaluation of GCM simulations (Patnaude et al., 2021; Yip et al., 2021; Maciel et al., 2023). Lastly, observation and simulation data for cloud fraction, LWP, IWP, and radiation are all averaged to hourly samples for direct comparisons.

3. Results

3.1 Cloud and radiative properties in MICRE and AWARE based on case studies and year-long observations

Case studies of cloud and radiative properties are conducted for selected days during the MICRE and AWARE campaigns (Figures 1 and 2). Both case studies feature an extratropical cyclone track in close proximity to the respective station locations. A convective cloud system was selected for the MICRE case study, while a low-level stratiform cloud system was selected for AWARE case study. The case studies allow for examinations of the responses of cloud and radiation properties to the nearby cyclones in two different types of cloud systems. A series of variables are examined, including cloud fraction, cloud phase, LWP, IWP, and net surface radiation. The synoptic conditions are also examined using the Worldview satellite images based on Terra/MODIS base layer taken at 00:00 UTC on each day of the respective case study. Sea level pressure maps at 6-hourly frequency are also shown. Both CAM6 and EAMv1 simulations can capture the temporal variability in cloud fraction for both cases.

The case study of the MICRE campaign spans from January 12, 2017, 12:00 UTC to January 15, 2017, 12:00 UTC. When examining the Worldview images and sea level pressure maps (Figures 1a–1f), frontal cloud bands passed through the Macquarie Island shortly after 00:00 UTC on January 13, leading to an increasing trend of cloud fraction and LWP as shown in the observations (Figure 1g and 1j). The center of an extratropical cyclone passed by Macquarie Island around 22:00 UTC on January 14. Both CAM6 and EAMv1 show similar increasing trends of cloud fraction, LWP, and IWP as seen in the observations starting from 08:00 UTC January 13 (Figure 1g–1j), as part of a convective system. Based on the vertical profiles of simulated cloud phases (Figure 1h and 1i), this convective cloud has an ice layer up to 10 km, a mixed-phase layer from surface to 6 km and a liquid layer below 2 km. However, both simulations underestimate IWP and overestimate LWP from 18:00 UTC January 13 to 03:00 UTC January 14 (Figure 1j). The overestimated LWP likely leads to the higher reflected SW radiation in the simulations around that time, which results in lower net surface SW radiation in the simulations (Figure 1k). The observations show a net gain of surface LW radiation from 08:00 to 20:00 UTC on January 13 (i.e., local nighttime 18:00 pm on January 13 to 6:00 am on January 14 in Australian Eastern Standard Time), which is opposite to the net loss of surface LW radiation in the simulations (Figure 1l). This is likely caused by the underestimation of IWP by simulations, which leads to underestimation of the warming effect of clouds on Earth's surface especially during local nighttime in this case study. Comparing the sea level pressure maps between NCEP reanalysis data and simulations, only small differences are seen in the trajectory of the low-pressure center of the extratropical cyclone and the overall sea level pressure distributions.

The AWARE campaign case study spans from March 11, 2016, 12:00 UTC to March 14, 2016, 12:00 UTC (Figure 2). An extratropical cyclone was seen moving eastward around 60°S, which is ~15° north of the latitudinal location of McMurdo Station (Figure 2a–2f). Similar to the MICRE case study, the simulated sea level pressure maps show very similar synoptic conditions to NCEP data during this three-day period. Both simulations show a low-level stratiform cloud, similar to the thickness of a low cloud observed by the combined lidar and radar measurements (Figure 2g–2i). The vertical profiles of cloud layers show a thick liquid layer in CAM6 between surface and 4 km and a thick mixed-phase layer in EAMv1 between 1 – 3 km that are not seen in the observed profiles (Figure 2h and 2i). CAM6 and EAMv1 both overestimate LWP from 18:00 UTC March 11 to 12:00 UTC March 12 (Figure 2j), while the simulated IWP are much lower than the observed values. The competition of these two biases leads to simulated surface net SW being not significantly different from the observed values (Figure 2f). Around 00:00 UTC March 13, both simulations significantly underestimate LWP and IWP, which leads to a positive bias in net SW and a negative bias in net LW radiation at surface.

Using monthly-averaged datasets spanning the entire campaigns, the seasonal variability of cloud and radiative properties are contrasted among observations, reanalysis, and model simulations (Figure 3). The differences between various datasets for monthly averaged variables are shown in Figure S1 in the supplemental material. Figure 3 is the only analysis using monthly averages while the rest of the tables and figures shown in the main text are based on 1-hour resolution data. The standard deviations of variables within each month are also illustrated for each bin. Sea level pressure values are similar between NCEP data and GCM simulations for both MICRE and AWARE, with small differences of a few hPa to up to 5 hPa (Figure 3a and 3b). The seasonal variability of sea level pressures is similar between MICRE and AWARE data, which both show lower values in January and September as well as higher values in April and November. Cloud fraction in MICRE is close to 1, while the monthly average cloud fraction in AWARE ranges from 0.5 to 0.9 (Figure 3c and 3d). The simulated cloud fractions by CAM6 and EAMv1 are slightly higher than the observed values for the MICRE campaign (by 0.05), while the simulated cloud fractions by two models are lower than the observed values for AWARE (by 0.1 – 0.4). The simulated LWP by both models shows large positive biases in MICRE and small negative biases in AWARE, except for December and January in AWARE showing positive LWP biases (Figure 3e and 3f). For IWP biases, both models show negative IWP biases at both locations, underestimating IWP by 0.5 – 1 order of magnitude. Based on the vertical profiles of RHice and RHliq from radiosonde observations and model simulations (Figure 4), CAM6 and EAMv1 show higher RHice and RHliq than observations for AWARE, which indicates that the lack of water vapor supply may not explain the underestimated cloud fraction, LWP, and IWP in AWARE by the two models. This type of comparison is limited to AWARE since radiosonde data were not available for MICRE.

Regarding radiative biases, the seasonal variability of net surface SW radiation is clearly seen in both observations and simulations (Figure 3i and 3j). Both simulations overestimate the net surface SW radiation by 10 – 30 W m^{-2} in austral spring and summer (i.e., September – February), and show smaller biases (less than 10 W m^{-2}) for austral fall and winter (Figure S1 i and j). For net surface LW radiation in MICRE (Figure 3k), the observations show slightly positive net surface LW from January to April, followed by more negative LW values for the rest of the year. Both simulations show net surface LW consistently being negative and closer to zero, with smaller seasonal variability than the observed trend. For the AWARE campaign (Figure 3l), the simulated net surface LW values are more comparable to the observed values for most time of the year (i.e., February to October) with relatively small negative model biases within ±10 W m^{-2}. For the austral summer in AWARE, the LW biases become positive and larger, which are up to +50 W m^{-2} (Figure S1 k and l). Comparing the two models, similar directions and magnitudes of biases are seen in each variable for both sites, except for CAM6 showing slightly smaller biases in cloud fraction and LWP for AWARE compared with EAMv1.

Overall, the main cloud biases in simulations are the positive cloud fraction and LWP biases in MICRE, negative cloud fraction and LWP biases in AWARE, and negative IWP in both campaigns. The dry biases of the simulations in AWARE are consistent with previous studies such as Silber et al. (2019a), Hines et al. (2019), and Yip et al. (2021) in the McMurdo region. In the above analyses of case studies and monthly averages during MICRE and AWARE campaigns, correlations between model biases in cloud properties and surface radiation are seen, the correlations of these biases with dynamical conditions will be further examined in the following sections. Previous studies have reported that the climatology of clouds at McMurdo is strongly influenced by mesoscale dynamics and forcing (e.g., Carrasco & Bromwich, 1993; Carrasco et al., 2003; Jolly et al., 2018; Silber et al., 2019b). But since mesoscales are often too fine for GCMs simulations to represent, we focus on the analysis of the role of synoptic conditions in this study.

3.2 Identifications of extratropical cyclone centers using a cyclone compositing method

The positions of extratropical cyclones (low-pressure systems) are identified using the NCEP reanalysis data for every 6 hours in 2016 and 2017 (Figure 5). An algorithm was developed to locate the centers of extratropical cyclones. The algorithm detects the sea level pressure minimum at each time stamp within a ±30° × 30° latitudinal and longitudinal box surrounding respective station locations. The size of the box was selected to ensure that the locations of extratropical cyclones are not too far away from the station location and a sufficient number of samples can be provided. In fact, we tested several different sizes of the boxes, such as ±15°×15°, ±30°×30°, and

±60°×60°, and finally chose ±30°×30° surrounding each station. The sea level pressure minimum identified represents the extratropical cyclone center. A manual inspection of the cyclone centers was applied to verify that this algorithm can capture the eastward trajectories of cyclones. The spatial distributions of cloud and radiation properties at each station are then analyzed relative to the extratropical cyclone centers.

Figure 5a and 5b show the latitude and longitude distributions of extratropical cyclones for MICRE and AWARE, respectively, with the highest number of extratropical cyclones located around two clusters – 63°S, 180°E and 67°S, 180°E, and a secondary peak at 120°E for both sites. The geographical locations of extratropical cyclones are similar between the two campaigns even though they sampled different years. Both campaigns show extratropical cyclones moving eastward and poleward, consistent with the previous study of Hoskins & Hodges (2005) which showed that cyclonic systems spiraled poleward from lower latitudes to Antarctica. The seasonal distributions of extratropical cyclones are displayed on geographic maps (Figures 5c–5f), including December, January, and February (DJF), March, April, and May (MAM), June, July, and August (JJA), and September, October, and November (SON). The locations of extratropical cyclones using pressure output from the two model simulations are also shown in Figures S2 and S3 in the supplemental material.

A relative coordinate system is developed to identify each station's position relative to the nearby extratropical cyclone centers. The "L" at (0, 0) position of this coordinate system (as shown in Figures 6 and 7) marks the center of each extratropical cyclone. Latitudinal and longitudinal differences between each ground station and the nearest extratropical cyclone within 6 hours are shown as the ordinate and abscissa, respectively. Four quadrants of the relative positions of a ground station with respect to the low-pressure system centers are defined as quadrants 1, 2, 3 and 4 (Q1 – Q4). These quadrants represent cases when a ground station is at the northeast, northwest, southwest, and southeast side of an extratropical cyclone, respectively. The definition of four quadrants follows the conventional definition used by previous studies of cyclone compositing, such as a schematic map illustrated in Bodas-Salcedo et al. (2014) in their Figure 3a1, and in Tansey et al. (2022) in their Figure 1. Among the four quadrants, Q1 (northeast) is considered the frontal region also known as the warm-air sector, as illustrated in Bodas-Salcedo et al. (2012) in their Figure 6, and in Montoya Duque et al. (2022) in their Figure 1. Different methods have been used to contrast different regions surrounding the extratropical cyclones. Lang et al. (2018) and Montoya Duque et al. (2022) used the k-mean clustering techniques to separate the four quadrants and their surrounding regions into 7 detailed categories. Bodas-Salcedo et al. (2012, 2014) contrasted the warm (Q1) and cold sectors (Q2-4). Another study by Kelleher and Grise (2019) developed dynamical regimes using mid-tropospheric vertical velocity (ω) and estimated inversion strength (EIS) and showed distinct differences in these variables in four quadrants surrounding extratropical cyclones, especially between the eastern sector (Q1 and Q4) and western sector (Q2 and Q3). Their study showed that the eastern sector of the cyclone (particularly Q1 in frontal region) is mainly associated with negative anomalies of pressure vertical velocity (i.e., $\omega' < 0$) relative to multi-year daily mean values, indicating rising air motion on the large scale, while the western sector of the cyclone is mainly associated with positive anomalies of vertical velocity (i.e., $\omega' > 0$), indicating subsiding motion on the large scale. Thus, in the rest of the analysis we contrast the two sectors of the cyclones based on their distinct differences in large-scale vertical motion.

Vertical profiles of temperature, RHice, and RHliq are contrasted between the western and eastern sectors in Figure 4. In addition, distributions of the mid-tropospheric vertical velocity at 500 hPa (ω_{500}', defined as *d*Pressure/*d*time) are analyzed in supplemental Figure S4. Here ω_{500}' is calculated as the daily mean anomaly by subtracting the 10-day average ω_{500} values surrounding each daily ω_{500} value. In MICRE, the eastern sector is seen to be warmer and moister and associated with ascent motion, while the western sector is colder and drier and associated with descent motion. The warmer and moister air in the eastern sector in MICRE is consistent with the rising air motion seen in Kelleher and Grise (2019), and is also consistent with the advection of moist, warm air into this sector as discussed in Field and Wood (2007) and Tansey et al. (2022). On the other hand, AWARE shows smaller differences in ω_{500}' between two sectors, and its eastern sector is seen to be warmer and drier. Comparing the distance to the low-pressure centers, MICRE is closer to the low-pressure centers with distance less than 15° in latitude, while AWARE is farther from the low-pressure centers with distance larger than 15° in latitude. This may explain why AWARE shows warmer but drier air in the eastern sector, with reduced influences from cyclones. The diminishing influences of extratropical cyclones with increasing distances are also shown in Tansey et al. (2022).

3.3 Spatial distributions of cloud and radiation properties in a dynamic coordinate relative to the cyclone centers

Cloud properties (i.e., cloud fraction, LWP, and IWP) and surface net radiation in SW and LW are examined in this relative coordinate system for the entire dataset of MICRE (Figure 6) and AWARE (Figure 7). For the MICRE campaign in Figure 6, both observations and simulations show that the majority of cloud fraction data have values close to 1 in all four quadrants (Figure 6 column 1), consistent with the monthly average values being close to 1 shown in Figure 3c. For the observations in AWARE, larger asymmetries between the western (i.e., Q3) and eastern (i.e., Q4) sector of the extratropical cyclones are seen in cloud fraction and LWP (Figure 7 bottom row) compared with MICRE (Figure 6 bottom row), while IWP is more symmetric at both sites. Higher LWP in the western sector (post-frontal) of the cyclones are seen in both MICRE and AWARE observations, which is consistent with previous studies (e.g., Bauer and Del Genio, 2006; Naud et al., 2006), since this is a cold-air region with descending air motion, often producing extensive coverage of closed-cell cumulus with high amount of supercooled liquid water that can eventually develop into congestus clouds.

Both CAM6 and EAMv1 simulations capture similar asymmetrical distributions of cloud fraction, LWP, and net SW and LW between two sectors of the cyclones in AWARE and MICRE, indicating that the relationships between these properties and extratropical cyclones are well represented in the models at both locations. In addition, both simulations are able to represent the relatively smaller cloud fraction, LWP, and IWP at AWARE compared with MICRE. The main cloud biases for both models are the consistent underestimation of IWP at both sites. In MICRE, both CAM6 and EAMv1 simulations show higher LWP than the observations in two sectors (Figure 6q). In AWARE, both models underestimate cloud fraction in the eastern sector and underestimate LWP in two sectors. For the radiation biases, the two models show different biases for net SW and net LW between MICRE and AWARE. That is, two models show negative biases of both net SW and LW in MICRE and positive biases of them in AWARE. The differences in radiation biases may be related to the variations in cloud biases between two sites, such as the variations in cloud fraction biases and LWP biases.

3.4 Comparisons of cloud and radiation properties in western and eastern sectors of extratropical cyclones

To assess whether the asymmetrical or symmetrical distributions of the cloud and radiation properties between two sectors of the cyclones are statistically significant, distributions of a series of quantities are compared between the two regimes (i.e., the eastern sector with more frontal influences versus the western sector with more post-frontal influences), including cloud fraction, LWP, IWP, and net SW and LW radiation at surface. In addition, the model biases for each of these properties are also contrasted (Table 1). Standard deviations of samples within each sector in Tables 1 and 2 are quantified in supplemental Tables S1 and S2. The two-tail t-tests with 95% confidence intervals are used to assess the statistical significance of their differences. The |T| values calculated for the t-test are listed, and those indicating statistically significant differences between two regimes are marked in italics. Quantities with higher values in the eastern sector of the cyclones are marked with an underscore. Overall, AWARE campaign shows that 18 out of 25 quantities have statistically significant differences between the two sides (marked with italics in Table 1 last column). In addition, 5 out of 25 quantities in AWARE show higher values in the eastern sector of the cyclones (marked with underscores in Table 1 last column). The observed IWP is the only observed quantity showing no statistically significant difference between the two sectors and also is the only observed quantity showing a higher average value in the eastern sector.

Compared with the AWARE campaign which shows significantly different cloud fraction and LWP in two dynamic regimes based on the observations, the observed quantities in the MICRE campaign show no statistically significant differences in them. CAM6 also shows no statistically significant differences in these two quantities, while EAMv1 shows a higher cloud fraction in the western side and higher LWP in the eastern sector. Comparisons of IWP show more inconsistencies between models and observations, with either one or both models showing the opposite asymmetry of IWP at two sites.

The asymmetrical distributions in net SW and LW are mostly consistent between observations and simulations for AWARE, except for CAM6 showing the opposite asymmetry for net LW compared with observations. For MICRE, both models show the same asymmetry in net LW as that observed, but show opposite asymmetry in net SW, i.e., the observations show higher SW (statistically significant) in the western sector and two models show higher SW (not statistically significant) in the eastern sector. As for model biases in SW and LW, the domain average dSW of two models are -4.15–4.07 W m^{-2} for MICRE and 11.65–13.16 W m^{-2} for AWARE. The domain averages of dLW in MICRE and AWARE are -11.63–0.37 W m^{-2} and 1.72–8.94 W m^{-2}, respectively. In previous model evaluation studies, the asymmetrical distributions of model biases have been a major issue related to the severe underestimation of supercooled liquid water in the climate models (Bodas-Salcedo et al. 2012, 2014; Williams et al. 2013; Naud et al. 2014). This is because the cold-air, post-frontal region that is dynamically suppressed provides a favorable condition for persistent low-level clouds containing supercooled-cooled liquid water. The fact that this model evaluation study finds more similar asymmetrical distributions in SW and LW between models and observations in the two sectors is consistent with the model improvements in cloud microphysics parameterizations as discussed in D'Alessandro et al. (2019), Yang et al. (2021) and Desai et al. (2023), i.e., the CAM6 and EAMv1 models now allow more supercooled liquid water to occur compared with older model versions, and therefore reduce the positive biases of net absorbed SW in the cold post-frontal sector.

Table 2 shows another type of comparison of observed and simulated quantities in different dynamical regimes using ω_{500}'. The samples are separated into two regimes, i.e., $\omega_{500}' > 0$ and $\omega_{500}' \leq 0$. As mentioned previously, the warm frontal eastern sector is more associated with ascent motion, i.e., $\omega_{500}' \leq 0$, while the cold post-frontal western sector is more associated with descent motion, i.e., $\omega_{500}' > 0$ as shown in Kelleher & Grise (2019) in their Figure 3. As a result, the main asymmetrical distributions between descending and ascending regions in Table 2 are comparable to those seen between the western and eastern sectors in Table 1, respectively. For example, the observations in AWARE campaign show statistically significant differences in all the quantities between the two dynamic regimes, including cloud fraction, LWP, IWP, and net SW and LW radiation. The observations in MICRE only show statistically significant differences in net LW but not in other quantities. Note that the dynamical regimes of $\omega_{500}' > 0$ and $\omega_{500}' \leq 0$ do not fully align with the separation between western and eastern sectors, since part of the western (eastern) sector still shows $\omega_{500}' \leq 0$ ($\omega_{500}' > 0$). This likely causes the results in Tables 1 and 2 to be not identical.

Weighted root mean square error (RMSE) is calculated for each model variable to examine the model performance for simulating different variables (Figure 8). The weighted RMSE is calculated as the square root of the mean differences between simulated and observed quantities, normalized by the standard deviation of the observed quantity. Quantities with statistically significant differences between the two sectors of the cyclones (i.e., italics in Table 1) are illustrated with filled markers. A total of 11 out of 20 variables show statistically significant differences between the two sectors. The markers located above and below the 1:1 line indicate higher RMSE values in the western and eastern sector, respectively. About half of the variables are very close to the 1:1 line, and the rest of the quantities show a similar number of points being higher in one sector than the other. The curved thin black lines illustrate the multiplication of the two weighted RMSE values on the two sectors of the cyclones. Markers located at the top-right (bottom-left) corners indicate those values in simulations with larger (smaller) discrepancies compared with the observations. Comparing the two simulations, the LWP biases of CAM6 and EAMv1 in MICRE have the largest RMSE, followed by cloud fraction biases of AWARE and IWP biases at both locations. In addition, CAM6 shows higher RMSE than EAMv1 for both SW and LW AWARE, as well as higher LW and LWP biases in MICRE. The smallest model RMSE values are seen in net SW radiation in AWARE, possibly due to the smaller solar radiation at higher latitudes as well as relatively smaller biases of LWP in AWARE compared with MICRE.

3.5 Diagnosis of factors contributing to radiation biases in simulations

The impacts of multiple factors on the model simulations of net surface SW and LW radiation are investigated, including cloud properties and seasonal variability. The seasonal variability of net radiation is shown in Figures 9 and 10. Linear regressions are applied to the simulated versus observed values, with slope values (b) and coefficient of determination (r^2) values shown in figure legends. Comparing the two campaigns, the slope values of net surface SW radiation for MICRE for all seasons are 0.894 and 0.907 for CAM6 and EAMv1, respectively (Figure 9a and 9b), which have larger deviation from the 1:1 line than the slope values for AWARE (0.949 and 1.007 in Figure 9c and 9d). The r^2 values of net surface SW radiation are also lower in MICRE (0.710 and 0.764 for CAM6 and EAMv1, respectively) than those in AWARE (0.780 and 0.901).

For net surface LW radiation (Figure 10), the b values are in the range of 0.2 – 0.5 and r^2 values are in the range of 0.1 – 0.5. For CAM6 and EAMv1, b values are 0.354 and 0.374 in MICRE and 0.271 and 0.340 in AWARE; r^2 values are 0.199 and 0.280 in MICRE and 0.182 and 0.313 in AWARE, respectively. The two modes seen in Figure 10c and d become one mode when analyzing columns without cloud layers, but the two modes are still seen for cloudy-sky conditions, suggesting that these two modes may be caused by different types of clouds. Comparing the two models, EAMv1 shows slightly better results than CAM6 when analyzing net SW and LW radiation in almost all seasons, with the exception of LW radiation in MICRE, where two models show similar results. Overall, net surface LW shows larger deviation from the 1:1 line and larger seasonality in the biases compared with net SW, consistent with monthly averages in Figure 2.

To further diagnose the effects of cloud properties on simulated radiative properties, slope b and r^2 values from linear regressions of net surface SW and LW are further shown for various ranges of observed cloud properties (i.e., observed cloud fraction, LWP, and IWP) and model biases in cloud properties (i.e., dCF, dLWP, and dIWP) in Table 3. For various cloud fractions, the conditions closer to clear sky (cloud fraction < 0.1) show the highest slope and r^2 values for almost all SW and LW linear regressions at both sites, which means that both CAM6 and EAMv1 have better simulations of net surface radiation when observations are closer to clear-sky conditions. When examining the correlations with observed LWP, better model performance (i.e., slope closer to 1) for both SW and LW linear regressions are seen when observed LWP are lower than 0.05 kg m^{-2}, indicating that clouds containing smaller mass concentrations of liquid hydrometeors tend to be represented better for their radiative effects in the two models. Similarly, when examining the correlations with simulated biases of cloud properties, the smaller values of dCF (within $\pm$ 0.5) and dLWP (within $\pm$ 0.1 kg m^{-2}) are associated with linear regression slopes closer to one. On the other hand, for various ranges of observed IWP, the linear regressions of model simulations do not necessarily show better results when IWP values are at a specific range. This result may be caused by the fact that the model simulations often show negative biases in IWP on 0.5 – 1 orders of magnitudes, which is a persistent bias regardless of the observed value. This is corroborated by the fact that the model simulations show linear regression slopes closer to one in the dIWP range of -0.1 to 0 kg m^{-2} compared with those in the dIWP range of -0.1 to -0.5 kg m^{-2}.

The correlations between radiative biases (dSW and dLW) and cloud property biases are examined for two sectors, including correlations with dCF, dLWP and dIWP in Figures 11 – 13, respectively. The signs of the linear correlation slopes (positive or negative) between radiative biases and three cloud property biases are consistent between two simulations, as well as being consistent between two campaigns. That is, dSW is negatively correlated with dCF, dLWP, and dIWP (Figures 11 – 13 rows 1 and 3), and dLW is positively correlated with dCF, dLWP and dIWP (rows 2 and 4). However, one should note that the r^2 values are very small for most linear regressions, possibly due to other factors besides cloud biases that also contribute to the net radiation biases. Even though the misrepresentation of cloud properties is not necessarily the same between two sites or between the two simulations, the correlations between model biases in cloud properties and biases in radiation are more consistent. This feature indicates that the fundamental physical mechanisms controlling cloud-radiation relationships are similar between the two models.

Contrasting the two sectors, the stronger correlations between radiative and cloud biases (i.e., r^2 values closer 1) do not always occur in one sector compared with the other sector. In addition, the correlations of radiative biases with dIWP all show much lower r^2 values, because the radiative biases can be either negative or positive while dIWP show more negative values. These lower r^2 values do not suggest that dIWP is not an important factor for radiative biases, but rather suggest that simulated IWP are consistently too low than the observed values regardless of the radiative biases, which is consistent with the findings in Table 3. The consistent low biases of IWP are also shown in supplemental Figure S5 for the correlations between dIWP and dLWP. The figure shows that dIWP are almost exclusively negative, while dLWP can be both positive and negative. In addition, weak positive correlations between dIWP and dLWP are seen in both MICRE and AWARE for both model simulations, suggesting that negative biases of dIWP do not necessarily correlate with positive biases of dLWP. This result indicates that the lack of ice phase clouds may partly originate from the lack of ice nucleation and/or ice growth and is not limited to errors in phase partitioning.

An additional analysis focusing on the downwelling component of the LW radiation is shown in Figure S6. The linear regressions between observed and simulated values for downwelling LW radiation shows r^2 values closer to 1 for both MICRE and AWARE, and also show b values closer to 1 for AWARE, compared with the net LW radiation linear regressions in Figure 8. The closer match between simulated and observed downwelling LW radiation is likely caused by other factors influencing the net LW radiation, such as surface temperatures and land-energy partitioning affecting LW cooling, latent heat fluxes, and sensible heat fluxes. In addition, the supplemental Figure S7 shows the relationships between model biases in downwelling LW radiation and model biases in cloud properties. Similar to the directions of the relationships between net LW biases and cloud biases seen in Figures 11 – 13, positive correlations are seen for downwelling LW biases with respect to dCF, dLWP, and dIWP. For the r^2 values in the linear regressions against dCF, analysis of downwelling LW biases shows r^2 values slightly closer to 1 compared with the analysis of net LW biases, but the r^2 values are not always closer to 1 when analyzing downwelling LW biases against dLWP and dIWP.

4. Summary, Conclusions, and Implications

The polar regions are experiencing disproportionate warming compared with the rest of the globe. Thus, accurately representing radiative forcing for the polar regions in climate models has become an urgent task. In this work, we compared the ground-based measurements of clouds and radiation with the simulations of two GCMs – the NCAR CESM2/CAM6 and DOE E3SM/EAMv1. Synoptic conditions at two ground sites – McMurdo Station and Macquarie Island were also contrasted, especially focusing on the variations of cloud and radiative properties in different quadrants relative to the center of extratropical cyclones. The analysis helps to shed light on the influence of synoptic conditions on cloud and radiative properties from lower to higher southern latitudes. Various factors that may contribute to model biases in net surface SW and LW radiation were also diagnosed.

The influences of synoptic conditions on clouds and radiation were examined at each site. A cyclone compositing method was used to track the low-pressure centers of extratropical cyclones as they propagated across the two sites (Figures 5–7). When evaluating the relationships of dynamics-cloud-radiation in AWARE, both models capture the asymmetrical distributions of most cloud and radiative properties between two sectors of the cyclones (Table 1). That is, observations and two simulations in AWARE show statistically significant differences between the two sectors of the cyclones for cloud fraction, LWP, and net surface SW and LW radiation (Table 1). One exception is that CAM6 shows the opposite asymmetry for LW radiation in AWARE. In addition, most of these quantities have higher values in the western sector of the cyclones in the AWARE campaign, i.e., the post-frontal region with subsiding air. Some exceptions include the observed IWP and CAM6 simulated LW being higher in the eastern sector.

The MICRE observations on the other hand show symmetric cloud fraction and LWP between the two sectors, while IWP and net SW and LW radiation are more asymmetric between two sectors. The two simulations captured the asymmetry in LW radiation in MICRE but at least one or both models misrepresent the asymmetry of other cloud variables. The main model biases in MICRE include the overestimations of cloud fraction and LWP and the underestimations of LW radiation in both sectors, as well as the underestimation of net SW in the western sector (Figure 6). The main model biases in AWARE include the underestimations of cloud fraction and LWP, as well as the overestimations of net SW and LW radiation (Figure 7). For both sites, IWP values are consistently underestimated. The large cloud fraction biases in AWARE seen in Figure 8 may be caused by the strong mesoscale dynamical influences at the McMurdo Station including the katabatic winds as previously mentioned (e.g., Carrasco & Bromwich, 1993; Carrasco et al., 2003; Jolly et al., 2018; Silber et al., 2019b).

One of the main objectives of this work is to quantify the relationships between model biases of liquid and ice phase hydrometeors and synoptic-scale dynamics in both CAM6 and EAMv1, which are part of the CMIP6 project. Previously, analyses of older versions of models (e.g., models from CMIP3) have shown a significant overestimation of net absorbed SW at the top of the atmosphere in model simulations of cloudy conditions over the Southern Ocean (e.g., Trenberth and Fasullo, 2010), especially in the cold-air post-frontal regions of the extratropical cyclone (e.g., Bodas-Salcedo et al., 2012, 2014). Other studies have shown using satellite observations that the insufficient amount of supercooled liquid water in the models may be the main cause for such previously reported SW radiative biases in the older model versions (e.g., Kay et al., 2016; Frey and Kay, 2018; Tan et al., 2016; Tan & Storelvmo, 2016; Zhang et al., 2019, 2020). In this work, we found that the underestimation of supercooled liquid water in CAM6 and EAMv1 has been significantly improved, if not overcompensated. This result is consistent with the findings in McIlhattan et al. (2020), which evaluated CESM2 model simulations of Arctic clouds and precipitation and showed slight decrease of Arctic cloud ice and dramatic increase of liquid cloud water. In this study, a positive LWP bias around 0.1 kg m^{-2} (Figure S1 e) is shown at Macquarie Island, while a small negative LWP bias around 0.01 kg m^{-2} (Figure S1 f) is shown at McMurdo Station. A better representation of supercooled liquid water in the newer models was also previously shown in the observation-based evaluation by D'Alessandro et al. (2019) and Yang et al. (2021). Those two studies contrasted the CAM version 5 with CAM version 6 and showed significant improvements of allowing supercooled liquid water to occur below -10°C.

Compared with an improved representation of liquid phase, negative biases in IWP are consistently seen at both Macquarie Island (dIWP around -0.1 kg m^{-2}) and McMurdo Station (dIWP between -0.01 to -0.1 kg m^{-2}) (Figure S1). Both models consistently underestimate IWP by a factor of 3 – 10 in both dynamical sectors (Figures 6 and 7) as well as in four seasons (Figure 3). This finding is consistent with other evaluation studies of CAM6 and EAMv1 models, which also pointed out the underestimation of the ice phase in CAM6 and EAMv1 simulations over Southern Ocean and Antarctica (e.g., D'Alessandro et al., 2019; Yang et al., 2021; Yip et al., 2021; Desai et al., 2023; Zhao et al., 2023). This result indicates that these negative biases of IWP in CAM6 and EAMv1 have a weaker dependence on the dynamical forcings related to extratropical cyclones compared with the stronger dynamical dependence of insufficient supercooled liquid water previously reported for the older model versions. In addition, the analyses between radiative biases and cloud property biases (Figures 11 – 13) have two implications – first, improving the parameterizations of liquid hydrometeors from the older model versions are not sufficient to reduce all cloud-induced radiation biases; second, underlying issues still exist with parameterizations of ice hydrometeors (e.g., ice and snow), which may become one of the main causes of the simulated radiative biases in this region in the newer versions of models, as also suggested by previous studies (e.g., Cesana et al., 2021; Zhang et al., 2023).

Comparing the two models, CAM6 shows better agreement with the observations in terms of representing the symmetry in cloud fraction and LWP between two sectors at Macquarie Island (Table 1), while EAMv1 overestimates the asymmetry of these cloud properties by showing higher cloud fraction in the western sector and higher LWP in the eastern sector of the cyclones. On the other hand, when evaluating the RMSE in the models (Figure 8), CAM6 shows larger RMSE values for net SW and LW at both locations than EAMv1. Linear regressions of simulated radiative properties show slightly better comparison results (i.e., slope values closer to 1) by EAMv1 compared with CAM6 (Figures 9 and 10). One factor that has not been investigated in this study is the nudging time scale. Gettelman et al. (2020) showed that using two nudging time scales – 24 hrs versus 1 hr to nudge the horizontal winds and temperature in CAM6, the 1-hr nudging method increases the simulated LWP by 50% and therefore increases cloud optical depth by 50%. However, the changes in IWP between the two nudging methods are minimal (6%) in that study. This indicates that the nudging time scale plays a significant role in controlling the cloud liquid microphysical properties in simulations but may not be able to compensate for the insufficient amount of simulated IWP.

One caveat of this study is the data availability and representativeness from two limited geographical locations due to the scarcity of ground-based observations in the high southern latitudes. At Macquarie Island, climatological studies of precipitation records have shown marked increases of precipitation and mean wind speed since 1970, which are consistent with the predicted regional trend of the sub-Antarctic regions in response to a changing global climate (Adams, 2009). Another observational study by Lang et al. (2018) also showed that cloud structure at Macquarie Island frequently resides within a shallow marine atmospheric boundary layer, which is a representative feature of Southern Ocean low-level clouds. Compared with Macquarie Island, the McMurdo station in Antarctica is associated with more extreme conditions such as very low temperature and humidity (Bromwich et al., 2012). McMurdo Station is also under stronger orographic influences by the nearby mountains and islands which produce higher katabatic winds than Macquarie Island with modest orography. Previous study by Silber, Verlinde, Cadeddu et al. (2019b) showed that the cloud properties at McMurdo may not fully represent statistical cloud properties of the entire Antarctic continent, but measurements from the McMurdo station still provides a highly valuable observational dataset over this remote region.

Overall, using ground-based observations from two DOE field campaigns in the southern hemisphere, this work investigates synoptic influences spanning over four seasons for each site. The results provide a different perspective compared with the frequently used spaceborne remote sensing measurements in this remote region. The insufficient amount of ice phase hydrometeors has been identified as a persistent bias in Southern Ocean and Antarctica. The combination of underestimated LWP and IWP at McMurdo, Antarctica may be the main cause of the more severe overestimations of absorption of solar radiation at the surface in this high-latitudinal region compared with the low-latitudinal regions. Further investigation on ice processes in the model parameterization is needed to diagnose the specific reasons for biases of ice phase in order to improve the accuracy of representations of cloud and radiative properties in the high southern latitudinal regions.

Acknowledgement

T. Barone, M. Diao, Y. Shi, and X. Liu would like to acknowledge the funding support from the DOE Atmospheric System Research (ASR) grant DE-SC0021211. T. Barone and M. Diao would also like to acknowledge the funding support by the U.S. National Science Foundation (NSF) Office of Polar Programs (grant #1744965), DOE RDPP grant DE-SC0023155, and DOE Climate Resilience Grant DE-SC0024439. T. Barone received the Walker Fellowship from San Jose State University. This research used resources of the National Energy Research Scientific Computing Center, which is a DOE Office of Science User Facility supported by the Office of Science of the U.S. Department of Energy under Contract No. DE-AC02-05CH11231 using NERSC award BER-ERCAP0019880 and ERCAP0025013. We show our utmost appreciation for the hard work of the individuals who contributed to the MICRE and AWARE field campaigns.

Open Research

Observation data are available from ARM Data Discovery (https://adc.arm.gov/discovery/). The observational datasets of DOE ARM MICRE and AWARE field campaigns can be accessed from the ARM data repository at: https://www.arm.gov/research/campaigns/osc2016micre (DOE ARM MICRE, 2024) and https://www.arm.gov/research/campaigns/amf2015aware (DOE ARM AWARE, 2024). The CAM6 and EAMv1 nudged simulation output for the MICRE and AWARE campaigns are stored in open archive at Mendeley Data (https://data.mendeley.com/) using https://doi.org/10.17632/vd6gdmnxvp.1 (Barone et al., 2023).

References

Adams, N. (2009). Climate trends at Macquarie Island and expectations of future climate change in the sub-Antarctic. Papers and Proceedings of the Royal Society of Tasmania, 143, 1–8. https://doi.org/10.26749/rstpp.143.1.1

Andreas, A., Dooraghi, M., Habte, A., Kutchenreiter, M., Reda, I., & Sengupta, M. (2018). Solar Infrared Radiation Station (SIRS), Sky Radiation (SKYRAD), Ground Radiation (GNDRAD), and Broadband Radiometer Station (BRS) Instrument Handbook. U.S. Department of Energy. DOE/SC-ARM-TR-025, https://www.arm.gov/publications/tech_reports/handbooks/sirs_handbook.pdf

Barone, T., Shi, Y., Zhao, X., Liu, X., Diao, M. Barone, T., & Silber I. Diao, M. (2023). MICRE and AWARE Campaign Model Simulations by EAMv1 and CAM6CAM6 and EAMv1 model simulations for DOE MICRE and AWARE campaigns. (Vol. V1). Mendeley Data, V1. https://doi.org/10.17632/vd6gdmnxvp.1.

Bauer, M., & DelGenio, A. D. (2006). Composite analysis of winter cyclones in a GCM: Influence on climatological humidity, J. Clim., 19, 1652–1672. https://doi.org/10.1175/JCLI3690.1

Bender, F. A., Charlson, R. J., Ekman, A. M. L., & Leahy, L. V. (2011). Quantification of Monthly Mean Regional-Scale Albedo of Marine Stratiform Clouds in Satellite Observations and GCMs. J. Appl. Meteor. Climatol., 50, 2139–2148, https://doi.org/10.1175/JAMC-D-11-049.1.

Bjordal, J., Storelvmo, T., Alterskjær, K., & Carlsen, T. (2020). Equilibrium climate sensitivity above 5 °C plausible due to state-dependent cloud feedback. Nat. Geosci. 13, 718–721 (2020). https://doi.org/10.1038/s41561-020-00649-1

Bodas-Salcedo, A., Williams, K. D., Field, P. R., & Lock, A. P. (2012). The surface downwelling solar radiation surplus over the Southern Ocean in the met office model: The role of midlatitude cyclone clouds. Journal of Climate, 25(21), 7467– 7486. https://doi.org/10.1175/JCLI-D-11-00702.1

Bodas-Salcedo, A., Williams, K. D., Ringer, M. A., Beau, I., Cole, J. N. S., Dufresne, J. L., et al. (2014). Origins of the solar radiation biases over the Southern Ocean in CFMIP2 models. Journal of Climate, 27(1), 41– 56. https://doi.org/10.1175/JCLI-D-13-00169.1

Bodas-Salcedo, A., Andrews, T., Karmalkar, A. V., & Ringer, M. A. (2016). Cloud liquid water path and radiative feedbacks over the Southern Ocean. Geophysical Research Letters, 43(20), 10938– 10946. https://doi.org/10.1002/2016GL070770

Bodas-Salcedo, A., Mulcahy, J. P., Andrews, T., Williams, K. D., Ringer, M. A., Field, P. R., & Elsaesser, G. S. (2019). Strong dependence of atmospheric feedbacks on mixed-phase microphysics and aerosol-cloud interactions in HadGEM3. Journal of Advances in Modeling Earth Systems, 11, 1735– 1758. https://doi.org/10.1029/2019MS001688

Bogenschutz, P. A., Gettelman, A., Morrison, H., Larson, V. E., Craig, C., & Schanen, D. P. (2013). Higher-order turbulence closure and its impact on climate simulations in the community atmosphere model. Journal of Climate, 26(23), 9655–9676. https://doi.org/10.1175/JCLI-D-13-00075.1

Bouttes, N., Gregory, J. M., Kuhlbrodt, T. & Suzuki, T. (2012). The effect of windstress change on future sea level change in the Southern Ocean. Geophys. Res. Lett., 39, L23602, doi:10.1029/2012GL054207.

Bromwich, D. H., Nicolas, J. P., Hines, K. M., Kay, J. E., Key, E. L., Lazzara, M. A., et al. (2012). Tropospheric clouds in Antarctica. Reviews of Geophysics, 50(1), RG1004. https://doi.org/10.1029/2011RG000363

Carrasco, J. F., & Bromwich, D. H. (1993). Mesoscale cyclogenesis dynamics over the southwestern Ross Sea, Antarctica. Journal of Geophysical Research, 98(D7). https://doi.org/10.1029/92jd02821

Carrasco, J. F., Bromwich, D. H., & Monaghan, A. J. (2003). Distribution and characteristics of mesoscale cyclones in the Antarctic: Ross Sea eastward to the Weddell Sea. Monthly Weather Review, 131(2). https://doi.org/10.1175/1520-0493(2003)131<0289:DACOMC>2.0.CO;2

Ceppi, P., Hwang, Y.-T., Frierson, D. M. W., & Hartmann, D. L. (2012). Southern Hemisphere jet latitude biases in CMIP5 models linked to shortwave cloud forcing. Geophysical Research Letters, 39(19), L19708. https://doi.org/10.1029/2012GL053115

Ceppi, P., Hartmann, D. L., & Webb, M. J. (2016). Mechanisms of the Negative Shortwave Cloud Feedback in Middle to High Latitudes. J. Climate, 29, 139–157, https://doi.org/10.1175/JCLI-D-15-0327.1.

Cesana, G., & Chepfer, H. (2013). Evaluation of the cloud thermodynamic phase in a climate model using CALIPSO-GOCCP. Journal of Geophysical Research: Atmospheres, 118(14), 7922–7937. https://doi.org/10.1002/jgrd.50376

Cesana, G. V., Ackerman, A. S., Fridlind, A. M., Silber, I., & Kelley, M. (2021). Snow Reconciles Observed and Simulated Phase Partitioning and Increases Cloud Feedback. Geophysical Research Letters, 48(20). https://doi.org/10.1029/2021GL094876

Cesana, G. V., Khadir, T., Chepfer, H., & Chiriaco, M. (2022). Southern Ocean Solar Reflection Biases in CMIP6 Models Linked to Cloud Phase and Vertical Structure Representations. Geophysical Research Letters, 49(22). https://doi.org/10.1029/2022GL099777

Chapman, C. C., Hogg, A. M. C., Kiss, A. E., & Rintoul, S. R. (2015). The dynamics of Southern Ocean storm tracks. Journal of Physical Oceanography, 45, 884– 903. https://doi.org/10.1175/JPO-D-14-0075.1

Collins, W. J., et al. (2011). Development and evaluation of an earth-system model—HadGEM2. Geosci. Model Dev., 4, 1051–1075, doi:10.5194/gmd-4-1051-2011.

D'Alessandro, J. J., Diao, M., Wu, C., Liu, X., Jensen, J. B., & Stephens, B. B. (2019). Cloud phase and relative humidity distributions over the Southern Ocean in austral summer based on in situ observations and CAM5 simulations. Journal of Climate, 32(10). https://doi.org/10.1175/JCLI-D-18-0232.1

D'Alessandro, J. J., McFarquhar, G. M., Stith, J. L., Diao, M., DeMott, P. J., McCluskey, C. S., et al. (2023). An Evaluation of Phase, Aerosol-Cloud Interactions and Microphysical Properties of Single- and Multi-Layer Clouds Over the Southern Ocean Using in Situ Observations From SOCRATES. Journal of Geophysical Research: Atmospheres, 128(15), e2023JD038610. https://doi.org/10.1029/2023JD038610

Danabasoglu, G., Lamarque, J.-F., Bacmeister, J., Bailey, D. A., DuVivier, A. K., Edwards, J., et al. (2020). The Community Earth System Model Version 2 (CESM2). Journal of Advances in Modeling Earth Systems, 12, e2019MS001916. https://doi.org/10.1029/2019MS001916

Delanoë, J., Protat, A., Vinson, J. P., Brett, W., Caudoux, C., Bertrand, F., du Chatelet, J. P., Hallali, R., Barthes, L., Haeffelin, M., & Dupont, J. C. (2016). BASTA: A 95-GHz FMCW

Doppler radar for cloud and fog studies. Journal of Atmospheric and Oceanic Technology, 33(5). https://doi.org/10.1175/JTECH-D-15-0104.1

Desai, N., Diao, M., Shi, Y., Liu, X., & Silber, I. (2023). Ship-based observations and climate model simulations of cloud phase over the Southern Ocean. Journal of Geophysical Research: Atmospheres, 128, e2023JD038581. https://doi.org/10.1029/2023JD038581

DOE ARM AWARE campaign. (2024). [Dataset], https://www.arm.gov/research/campaigns/amf2015aware

DOE ARM MICRE campaign. (2024). [Dataset], https://www.arm.gov/research/campaigns/osc2016micre

Eloranta, E. E. (2006). High spectral resolution Lidar. In Lidar (pp. 143–163). Springer-Verlag. .org/10.1007/0-387-25101-4_5

Essery, R. L. H., Best, M. J., Betts, R. A., Cox, P. M., & Taylor, C. M. (2003). Explicit representation of subgrid heterogeneity in a GCM land-surface scheme. J. Hydrometeor., 4, 530–543. .org/10.1175/1525-7541(2003)004<0530:EROSHI>2.0.CO;2

Field, P. R., & Wood, R. (2007). Precipitation and cloud structure in midlatitude cyclones. J. Climate, 20, 233–254. .org/10.1175/JCLI4396.1

Field, P. R., Bodas-Salcedo, A., & Brooks, M. E. (2011). Using model analysis and satellite data to assess cloud and precipitation in midlatitude cyclones. Quarterly Journal of the Royal Meteorological Society, 137(659), 1501– 1515. https://doi.org/10.1002/qj.858

Flynn, C. M., & Mauritsen, T. (2020). On the climate sensitivity and historical warming evolution in recent coupled model ensembles. Atmospheric Chemistry and Physics, 20(13). https://doi.org/10.5194/acp-20-7829-2020

Frey, W. R., & Kay, J. E. (2018). The influence of extratropical cloud phase and amount feedbacks on climate sensitivity. Climate Dynamics, 50(7–8), 3097–3116. https://doi.org/10.1007/s00382-017-3796-5

Gettelman, A., & Morrison, H. (2015). Advanced Two-Moment Bulk Microphysics for Global Models. Part I: Off-Line Tests and Comparison with Other Schemes. Journal of Climate, 28(3), 1268–1287. https://doi.org/10.1175/JCLI-D-14-00102.1

Gettelman, A., Morrison, H., Santos, S., Bogenschutz, P., & Caldwell, P. M. (2015). Advanced Two-Moment Bulk Microphysics for Global Models. Part II: Global Model Solutions and Aerosol–Cloud Interactions. Journal of Climate, 28(3), 1288–1307. https://doi.org/10.1175/JCLI-D-14-00103.1

Gettelman, A., Bardeen, C. G., McCluskey, C. S., Järvinen, E., Stith, J., Bretherton, C., et al. (2020). Simulating Observations of Southern Ocean Clouds and Implications for Climate. Journal of Geophysical Research: Atmospheres, 125(21). https://doi.org/10.1029/2020JD032619

Gleckler, P. J. (2005). Surface energy balance errors in AGCMs: Implications for ocean-atmosphere model coupling. Geophys. Res. Lett., 32, L15708, doi:10.1029/2005GL023061.

Golaz, J. C., Caldwell, P. M., Van Roekel, L. P., Petersen, M. R., Tang, Q., Wolfe, J. D., Abeshu, G., Anantharaj, V., Asay-Davis, X. S., Bader, D. C., Baldwin, S. A., Bisht, G., Bogenschutz, P. A., Branstetter, M., Brunke, M. A., Brus, S. R., Burrows, S. M., Cameron-Smith, P. J., Donahue, A. S., Deakin, M., Easter, R. C., Evans, K. J., Feng, Y., Flanner, M., Foucar, J. G., Fyke, J. G., Griffin, B. M., Hannay, C., Harrop, B. E., Hoffman, M. J., Hunke, E. C., Jacob, R. L., Jacobsen, D. W., Jeffery, N., Jones, P. W., Keen, N. D., Klein, S. A., Larson, V. E., Leung, L. R., Li, H. Y., Lin, W. Y., Lipscomb, W. H., Ma, P. L., Mahajan, S., Maltrud, M. E., Mametjanov, A., McClean, J. L., McCoy, R. B., Neale, R. B., Price, S. F., Qian, Y., Rasch, P. J., Eyre, J. E. J. R., Riley, W. J., Ringler, T. D., Roberts, A. F., Roesler, E. L., Salinger, A. G., Shaheen, Z., Shi, X. Y., Singh, B., Tang, J. Y., Taylor, M. A., Thornton, P. E., Turner, A. K., Veneziani, M., Wan, H., Wang, H. L., Wang, S. L., Williams, D. N., Wolfram, P. J., Worley, P. H., Xie, S. C., Yang, Y., Yoon, J. H., Zelinka, M. D., Zender, C. S., Zeng, X. B., Zhang, C. Z., Zhang, K., Zhang, Y., Zheng, X., Zhou, T., & Zhu, Q. (2019). The DOE E3SM coupled model version 1: Overview and evaluation at standard resolution, J. Adv. Model. Earth Sy., 11, 2089–2129, https://doi.org/10.1029/2018MS001603.

Golaz, J.-C., Larson, V. E., & Cotton, W. R. (2002a). A PDF-Based Model for Boundary Layer Clouds. Part I: Method and Model Description. Journal of the Atmospheric Sciences, 59(24), 3540–3551. https://doi.org/10.1175/1520-0469(2002)059%3C3540:APBMFB%3E2.0.CO;2

Golaz, J.-C., Larson, V. E., & Cotton, W. R. (2002b). A PDF-Based Model for Boundary Layer Clouds. Part II: Model Results. Journal of the Atmospheric Sciences, 59(24), 3552–3571. https://doi.org/10.1175/1520-0469(2002)059<3552:APBMFB>2.0.CO;2

Golaz, J.-C., Caldwell, P. M., Van Roekel, L. P., Petersen, M. R., Tang, Q., Wolfe, J. D., et al. (2019). The DOE E3SM coupled model version 1: Overview and evaluation at standard resolution. Journal of Advances in Modeling Earth Systems, 11, 2089–2129. https://doi.org/10.1029/2018MS001603

Govekar, P. D., Jakob, C., Reeder, M. J., & Haynes, J. (2011). The three-dimensional distribution of clouds around Southern Hemisphere extratropical cyclones. Geophysical Research Letters, 38(21), 1– 6. https://doi.org/10.1029/2011GL049091

Govekar, P. D., Jakob, C., & Catto, J. (2014). The relationship between clouds and dynamics in Southern Hemisphere extratropical cyclones in the real world and a climate model. Journal of Geophysical Research: Atmospheres, 119(11), 6609–6628. https://doi.org/10.1002/2013JD020699

Hande, L. B., Siems, S. T., Manton, M. J., & Belusic, D. (2012). Observations of wind shear over the Southern Ocean. Journal of Geophysical Research, 117, D12206. https://doi.org/10.1029/2012JD017488

Hines, K. M., & Bromwich, D. H., Wang, S.-H., Silber, I., Verlinde, J., and Lubin, D. (2019). Microphysics of summer clouds in central West Antarctica simulated by the Polar Weather

Research and Forecasting Model (WRF) and the Antarctic Mesoscale Prediction System (AMPS), Atmos. Chem. Phys., 19, 12431–12454, https://doi.org/10.5194/acp-19-12431-2019.

Hinkelman, L. M., & Marchand, R. (2020). Evaluation of CERES and CloudSat surface radiation fluxes over Macquarie Island, the Southern Ocean. Earth and Space Science, 7(9). https://doi.org/10.1029/2020EA001224

Hogan, R. J., Mittermaier, M. P., & Illingworth, A. J. (2006). The retrieval of ice water content from radar reflectivity factor and temperature and its use in evaluating a mesoscale model. Journal of Applied Meteorology and Climatology, 45(2). https://doi.org/10.1175/JAM2340.1

Holland, P. R., Jenkins, A., & Holland, D. M. (2010). Ice and ocean processes in the Bellingshausen Sea, Antarctica. J. Geophys. Res., 115, C05020, doi:10.1029/2008JC005219.

Hoskins, B. J., & Hodges, K. I. (2005). A new perspective on Southern Hemisphere storm tracks. Journal of Climate, 18(20), 4108– 4129. https://doi.org/10.1175/JCLI3570.1

Humphries, R.S., et al. (2023). Measurement report: Understanding the seasonal cycle of Southern Ocean aerosols. Atmospheric Chemistry and Physics, 23(6), 10.5194/acp-23-3749-2023. https://doi.org/10.5194/acp-23-3749-2023

Hwang, Y. T., & Frierson, D. M. W. (2013), Link between the double-intertropical convergence zone problem and cloud biases over the Southern Ocean, Proc. Natl. Acad. Sci. U.S.A., 110, 4935–4940, doi:10.1073/pnas.121302110

Iacono, M. J., Mlawer, E. J., Clough, S. A., & Morcrette, J. J. (2000). Impact of an improved longwave radiation model, RRTM, on the energy budget and thermodynamic properties of the NCAR Community Climate Model, CCM3. Journal of Geophysical Research, 105(D11), 14873– 14890. https://doi.org/10.1029/2000JD900091

IPCC, 2013: Climate Change. (2013). The Physical Science Basis. Contribution of Working Group I to the Fifth Assessment Report of the Intergovernmental Panel on Climate Change [Stocker, T.F., D. Qin, G.-K. Plattner, M. Tignor, S.K. Allen, J. Boschung, A. Nauels, Y. Xia, V. Bex and P.M. Midgley (eds.)]. Cambridge University Press, Cambridge, United Kingdom and New York, NY, USA, 1535 pp.

IPCC, 2023: Climate Change. (2023). Synthesis Report. Contribution of Working Groups I, II and III to the Sixth Assessment Report of the Intergovernmental Panel on Climate Change [Core Writing Team, H. Lee and J. Romero (eds.)]. IPCC, Geneva, Switzerland, pp. 35-115, doi: 10.59327/IPCC/AR6-9789291691647.Jolly, B., Kuma, P., McDonald, A., & Parsons, S. (2018). An analysis of the cloud environment over the Ross Sea and Ross Ice Shelf using CloudSat/CALIPSO satellite observations: The importance of synoptic forcing. Atmospheric Chemistry and Physics, 18(13). https://doi.org/10.5194/acp-18-9723-2018

Kalnay, E., et al. (1996). The NCEP/NCAR 40-Year Reanalysis Project. Bull. Amer. Meteor. Soc., 77, 437-471. https://doi.org/10.1175/1520-0477(1996)077%3C0437:TNYRP%3E2.0.CO;2

Kay, J. E., Bourdages, L., Miller, N. B., Morrison, A., Yettella, V., Chepfer, H., & Eaton, B. (2016). Evaluating and improving cloud phase in the Community Atmosphere Model version 5 using spaceborne lidar observations. Journal of Geophysical Research: Atmospheres, 121(8), 4162–4176. https://doi.org/10.1002/2015JD024699

Kelleher, M. K., & Grise, K. M. (2019). Examining Southern Ocean cloud controlling factors on daily time scales and their connections to midlatitude weather systems. Journal of Climate, 32(16), 5145–5160. https://doi.org/10.1175/JCLI-D-18-0840.1

Klein, S. A., & Hartmann, D. L. (1993). The seasonal cycle of low stratiform clouds, J. Clim., 6(8), 1587– 1606. https://doi.org/10.1175/1520-0442(1993)006%3C1587:TSCOLS%3E2.0.CO;2

Klein, S. A., Hall, A., Norris, J. R., & Pincus, R. (2017). Low-Cloud Feedbacks from Cloud-Controlling Factors: A Review. Surveys in Geophysics, 38(6). https://doi.org/10.1007/s10712-017-9433-3

Lang, F., Huang, Y., Siems, S. T., & Manton, M. J. (2018). Characteristics of the marine atmospheric boundary layer over the Southern Ocean in response to the synoptic forcing. Journal of Geophysical Research: Atmospheres, 123, 7799–7820. https://doi.org/10.1029/2018JD028700

Larson, V. E., Golaz, J.-C., & Cotton, W. R. (2002). Small-Scale and Mesoscale Variability in Cloudy Boundary Layers: Joint Probability Density Functions. Journal of the Atmospheric Sciences, 59(24), 3519–3539. https://doi.org/10.1175/1520-0469(2002)059<3519:SSAMVI>2.0.CO;2

Lau, N. C., & Crane, M. W. (1995). A satellite view of the synoptic-scale organization of cloud properties in midlatitude and tropical circulation systems, Mon. Weather Rev., 123, 1984–2006. https://doi.org/10.1175/1520-0493(1995)123%3C1984:ASVOTS%3E2.0.CO;2

Lau, N. C., & Crane, M. W. (1997). Comparing satellite and surface observations of cloud patterns in synoptic-scale circulation systems, Mon. Weather Rev., 125, 3172– 3189. https://doi.org/10.1175/1520-0493(1997)125%3C3172:CSASOO%3E2.0.CO;2

Liou, K. N. (1992). Radiation and cloud processes in the atmosphere (pp. 255–339). Oxford University Press.

Liu, X., Ma, P.-L., Wang, H., Tilmes, S., Singh, B., Easter, R. C., Ghan, S. J., & Rasch, P. J. (2016). Description and evaluation of a new four-mode version of the Modal Aerosol Module (MAM4) within version 5.3 of the Community Atmosphere Model, Geosci. Model Dev., 9, 505–522, https://doi.org/10.5194/gmd-9-505-2016.

Liu, Y. (2022). Impacts of active satellite sensors' low-level cloud detection limitations on cloud radiative forcing in the Arctic, Atmos. Chem. Phys., 22, 8151–8173, https://doi.org/10.5194/acp-22-8151-2022.

Long, C. N., & Shi, Y. (2006). The QCRad Value Added Product: Surface Radiation Measurement Quality Control Testing, Including Climatologically Configurable Limits. U.S. Department of Energy. DOE/SCARM-TR-074, https://www.arm.gov/publications/tech_reports/doe-sc-arm-tr-074.pdf

Long, C. N., & Shi, Y. (2008). An Automated Quality Assessment and Control Algorithm for Surface Radiation Measurements. The Open Atmosphere Science Journal, 2, 23–37, https://doi.org/10.2174/1874282300802010023

Lubin, D., Zhang, D., Silber, I., Scott, R. C., Kalogeras, P., Battaglia, A., et al. (2020). AWARE: The Atmospheric Radiation Measurement (ARM) West Antarctic Radiation Experiment. Bulletin of the American Meteorological Society, 101, E1069–E1091, https://doi.org/10.1175/BAMS-D-18-0278.1.

Mace, G. G. J., & Protat, A. (2018). Clouds over the Southern Ocean as observed from the R/V investigator during CAPRICORN. Part I: Cloud occurrence and phase partitioning. Journal of Applied Meteorology and Climatology, 57(8). https://doi.org/10.1175/JAMC-D-17-0194.1

Maciel, F. V., Diao, M., & Patnaude, R. (2023). Examination of aerosol indirect effects during cirrus cloud evolution. Atmospheric Chemistry and Physics, 23(2). https://doi.org/10.5194/acp-23-1103-2023

Maciel, F. V., Diao, M., & Yang, C. A. (2024). The Transition from Supercooled Liquid Water to Ice Crystals in Mixed-phase Clouds based on Airborne In-situ Observations, Atmos. Meas. Tech., . accepted, https://doi.org/10.5194/amt-2022-256.

Marshall, J., & Speer, K. (2012). Closure of the meridional overturning circulation through Southern Ocean upwelling, Nat. Geosci., 5(3), 171–180. https://doi.org/10.1038/ngeo1391

Marchand R. (2020). Macquarie Island Cloud and Radiation Experiment (MICRE) Field Campaign Report. Ed. by Robert Stafford, ARM user facility. DOE/SC-ARM-20-005. 10.2172/1602536.

McCoy, D. T., Hartmann, D. L., & Grosvenor, D. P. (2014a). Observed Southern Ocean cloud properties and shortwave reflection. Part I: Calculation of SW flux from observed cloud properties. J. Climate, 27, 8836–8857, https://doi.org/10.1175/JCLI-D-14-00287.1

McCoy, D. T., Hartmann, D. L., & Grosvenor, D. P. (2014b). Observed Southern Ocean cloud properties and shortwave reflection. Part II: Phase changes and low cloud feedback*. Journal of Climate, 27(23), 8858– 8868. https://doi.org/10.1175/jcli-d-14-00288.1

McCoy, D. T., Burrows, S. M., Wood, R., Grosvenor, D. P., Elliott, S. M., Ma, P.-L., Rasch, P. J., & Hartmann, D. L. (2015). Natural aerosols explain seasonal and spatial patterns of Southern Ocean cloud albedo, Sci. Adv., 1(6). https://doi.org/10.1126/sciadv.1500157

McCoy, D. T., Tan, I., Hartmann, D. L., Zelinka, M. D., & Storelvmo, T. (2016). On the relationships among cloud cover, mixed-phase partitioning, and planetary albedo in GCMs.

Journal of Advances in Modeling Earth Systems, 8(2), 650– 668. https://doi.org/10.1002/2015MS000589

McCoy, D. T., Field, P. R., Elsaesser, G. S., Bodas-Salcedo, A., Kahn, B. H., Zelinka, M. D., et al. (2019). Cloud feedbacks in extratropical cyclones: Insight from long-term satellite data and high-resolution global simulations. Atmospheric Chemistry and Physics, 19(2), 1147–1172. https://doi.org/10.5194/acp-19-1147-2019

McFarquhar, G. M., Bretherton, C. S., Marchand, R., Protat, A., DeMott, P. J., Alexander, S. P., et al. (2021). Observations of clouds, aerosols, precipitation, and surface radiation over the Southern Ocean. Bulletin of the American Meteorological Society, 102(4), E894– E928. https://doi.org/10.1175/BAMS-D-20-0132.1

McIlhattan, E. A., Kay, J. E., & L'Ecuyer, T. S. (2020). Arctic clouds and precipitation in the Community Earth System Model version 2. Journal of Geophysical Research: Atmospheres, 125, e2020JD032521. https://doi.org/10.1029/2020JD032521

Morris, V. R. (2006). Microwave Radiometer (MWR) Handbook. U.S. Department of Energy, DOE/SC-ARM-TR-016, doi:10.2172/1020715, https://www.osti.gov/biblio/1020715

Mitchell, J. F. B., Senior, C. A., & Ingram, W. J. (1989), CO2 and climate: A missing feedback? Nature, 341(6238), 132– 134. https://doi.org/10.1038/341132a0

Montoya Duque, E., Huang, Y., Siems, S. T., May, P. T., Protat, A., & McFarquhar, G. M. (2022). A characterization of clouds and precipitation over the Southern Ocean from synoptic to micro scales during the CAPRICORN field campaigns. Journal of Geophysical Research: Atmospheres, 127, e2022JD036796. https://doi.org/10.1029/2022JD036796

Murphy, D. M., & Koop, T. (2005). Review of the vapour pressures of ice and supercooled water for atmospheric applications. Quarterly Journal of the Royal Meteorological Society, 131(608), 1539–1565. https://doi.org/10.1256/qj.04.94

Naud, C. M., Del Genio, A. D., & Bauer, M. (2006). Observational constraints on the cloud thermodynamic phase in midlatitude storms, J. Clim., 19(20), 5273– 5288. https://doi.org/10.1175/JCLI3919.1

Naud, C. M., Del Genio, A. D., Bauer, M., & Kovari, W. (2010). Cloud vertical distribution across warm fronts in CloudSat-CALIPSO data and a general circulation model, J. Clim., 23, 3397– 3415. https://doi.org/10.1175/2010JCLI3282.1

Naud, C.M., Booth, J.F., & Del Genio, A.D. (2014) Evaluation of ERA-interim and MERRA cloudiness in the Southern Ocean. J. Climate, 27, no. 5, 2109-2124, doi:10.1175/JCLI-D-13-00432.1.

Posselt, D., Stephens, G., & Miller, M. (2008). CloudSat—Adding a new dimension to a classical view of extratropical cyclones, Bull. Amer. Meteor. Soc., 89, 599–609. https://doi.org/10.1175/BAMS-89-5-599

Patnaude, R., Diao, M., Liu, X., & Chu, S. (2021). Effects of thermodynamics, dynamics and aerosols on cirrus clouds based on in situ observations and NCAR CAM6. Atmospheric Chemistry and Physics, 21(3), 1835– 1859. https://doi.org/10.5194/acp-21-1835-2021

Rasch, P. J., S. Xie, P.-L. Ma, W. Lin, H. Wang, Q. Tang, S. M. Burrows, P. Caldwell, K. Zhang, R. C. Easter, et al. (2019), An Overview of the Atmospheric Component of the Energy Exascale Earth System Model, J. Adv. Model. Earth Syst., 11, 2377–2411, https://doi.org/10.1029/2019MS001629.

Raschke, E., Kinne, S., Rossow, W. B., Stackhouse Jr., P. W., & Wild, M. (2016). Comparison of radiative energy flows in observational datasets and climate modeling. Journal of Applied Meteorology and Climatology., 55, 93–117, https://doi.org/10.1175/JAMC-D-14-0281.1

Riihimaki, L., Gaustad, K., & Long, C. (2019). Radiative Flux Analysis (RADFLUXANAL) Value-Added Product: Retrieval of Clear-Sky Broadband Radiative Fluxes and Other Derived Values. U.S. Department of Energy. DOE/SC-ARM-TR-228, https://www.osti.gov/biblio/1808702

Schuddeboom, A. J., & McDonald, A. J. (2021). The Southern Ocean Radiative Bias, Cloud Compensating Errors, and Equilibrium Climate Sensitivity in CMIP6 Models. Journal of Geophysical Research: Atmospheres, 126(22). https://doi.org/10.1029/2021JD035310

Silber, I., Verlinde, J., Eloranta, E. W., & Cadeddu, M. (2018). Antarctic cloud macrophysical, thermodynamic phase, and atmospheric inversion coupling properties at McMurdo station: I. principal data processing and climatology. Journal of Geophysical Research: Atmospheres, 123(11), 6099–6121. https://doi.org/10.1029/2018JD028279

Silber, I., Verlinde, J., Wang, S.-H., Bromwich, D. H., Fridlind, A. M., Cadeddu, M., et al. (2019a). Cloud Influence on ERA5 and AMPS Surface Downwelling Longwave Radiation Biases in West Antarctica. Journal of Climate, 32(22), 7935–7949. https://doi.org/10.1175/JCLI-D-19-0149.1

Silber, I., Verlinde, J., Cadeddu, M., Flynn, C. J., Vogelmann, A. M., & Eloranta, E. W. (2019b). Antarctic Cloud Macrophysical, Thermodynamic Phase, and Atmospheric Inversion Coupling Properties at McMurdo Station—Part II: Radiative Impact During Different Synoptic Regimes. Journal of Geophysical Research: Atmospheres, 124(3), 1697–1719. https://doi.org/10.1029/2018JD029471

Stanford, M. W., Fridlind, A. M., Silber, I., Ackerman, A. S., Cesana, G., Mülmenstädt, J., Protat, A., Alexander, S., & McDonald, A. (2023). Earth-system-model evaluation of cloud and precipitation occurrence for supercooled and warm clouds over the Southern Ocean's Macquarie Island. Atmospheric Chemistry and Physics, 23(16), 9037–9069. https://doi.org/10.5194/ACP-23-9037-2023

Taljaard, J. J. (1972). Synoptic meteorology of the Southern Hemisphere, in Meteorology of the Southern Hemisphere, edited by D. J. Karoly and D. G. Vincent, pp. 139– 211, Am. Meteorol. Soc. DOI: 10.1007/978-1-935704-33-1_8

Tan, I., & Storelvmo, T. (2016). Sensitivity study on the influence of cloud microphysical parameters on mixed-phase cloud thermodynamic phase partitioning in CAM5. Journal of the Atmospheric Sciences, 73(2), 709–728. https://doi.org/10.1175/JAS-D-15-0152.1

Tan, I., Storelvmo, T., & Zelinka, M. D. (2016). Observational constraints on mixed-phase clouds imply higher climate sensitivity. Science, 352, 224–227. https://doi.org/10.1126/science.aad5300

Tansey, E., Marchand, R., Protat, A., Alexander, S. P., & Ding, S. (2022). Southern Ocean precipitation characteristics observed from CloudSat and ground instrumentation during the Macquarie Island Cloud & Radiation Experiment (MICRE): April 2016 to March 2017. Journal of Geophysical Research: Atmospheres, 127. e2021JD035370. https://doi.org/10.1029/2021jd035370

Tansey, E., Marchand, R., Alexander, S. P., Klekociuk, A. R., & Protat, A. (2023). Southern Ocean Low Cloud and Precipitation Phase Observed During the Macquarie Island Cloud and Radiation Experiment (MICRE). Journal of Geophysical Research: Atmospheres, 128(17), e2023JD039205. https://doi.org/10.1029/2023JD039205

Terai, C. R., Klein, S. A., & Zelinka, M. D. (2016). Constraining the low-cloud optical depth feedback at middle and high latitudes using satellite observations. Journal of Geophysical Research: Atmospheres. https://doi.org/10.1002/2016JD025233

Trenberth, K. E., & Fasullo, J. T. (2010). Simulation of present-day and twenty-first-century energy budgets of the southern oceans. J. Climate, 23, 440–454, https://doi.org/10.1175/2009JCLI3152.1

Tsushima, Y., Emori, S. Ogura, T., Kimoto, M., Webb, M. J., Williams, K. D., Ringer, M. A., Soden, B. J., Li, B., & Andronova, N. (2006). Importance of the mixed-phase cloud distribution in the control climate for assessing the response of clouds to carbon dioxide increase: a multi-model study. Climate Dyn., 27, 113–126, doi:10.1007/s00382-006-0127-7.

Turner, D.D., Lo, C., Min, Q., Zhang, D., & Gaustad, K. (2021). Cloud Optical Properties from the Multi-filter Shadowband Radiometer (MFRSRCLDOD): An ARM Value-Added Product. Ed. by Robert Stafford, U.S. Department of Energy. DOE/SC-ARM/TR-047. 10.2172/1020280.

Wang, D., Yang, C.A., & Diao, M. (2024). Validation of Satellite-based Cloud Phase Distributions Using Global-Scale In-Situ Airborne Observations, Earth and Space Science, 11, e2023EA003355. https://doi.org/10.1029/2023EA003355 .

Wang, Z., Siems, S. T., Belusic, D., Manton, M. J., & Huang, Y. (2015). A climatology of the precipitation over the Southern Ocean as observed at Macquarie Island. Journal of Applied Meteorology and Climatology, 54(12), 2321– 2337. https://doi.org/10.1175/JAMC-D-14-0211.1

Widener, K., Bharadwaj, N., & Johnson, K. (2012). Ka-Band ARM Zenith Radar (KAZR) Instrument Handbook. https://doi.org/10.2172/1035855

Williams, K., Bodas-Salcedo, A., Déqué, M., Fermepin, S., Medeiros, B., Jakob, C., et al. (2013). The transpose AMIP II experiment and its application to the understanding of Southern Ocean cloud biases in climate models. Journal of Climate, 26(10), 3258–3274. https://doi.org/10.1175/JCLI-D-12-00429.1

Xie, S., and Coauthors (2010). Clouds and more: ARM climate modeling best estimate data. Bull. Amer. Meteor. Soc., 91, 13–20, https://doi.org/10.1175/2009BAMS2891.1

Xie, S., Lin, W., Rasch, P. J., Ma, P.-L., Neale, R., Larson, V. E., et al. (2018). Understanding cloud and convective characteristics in version 1 of the E3SM atmosphere model. Journal of Advances in Modeling Earth Systems, 10, 2618–2644. https://doi.org/10.1029/2018MS001350

Yang, C. A., Diao, M., Gettelman, A., Zhang, K., Sun, J., Mcfarquhar, G., & Wu, W. (2021). Ice and supercooled liquid water distributions over the Southern Ocean based on in situ observations and climate model simulations. Journal of Geophysical Research: Atmospheres, 126(24), e2021JD036045. https://doi.org/10.1029/2021JD036045

Yip, J., Diao, M., Barone, T., Silber, I., & Gettelman, A. (2021). Evaluation of the CAM6 climate model using cloud observations at McMurdo Station, Antarctica. Journal of Geophysical Research: Atmospheres, 126, e2021JD034653. https://doi. org/10.1029/2021JD034653

Zelinka, M. D., Myers, T. A., McCoy, D. T., Po-Chedley, S., Caldwell, P. M., Ceppi, P., et al. (2020). Causes of higher climate sensitivity in CMIP6 models. Geophysical Research Letters, 47(1). https://doi.org/10.1029/2019GL085782

Zhang, M., Liu, X., Diao, M., D'Alessandro, J. J., Wang, Y., Wu, C., et al. (2019). Impacts of Representing Heterogeneous Distribution of Cloud Liquid and Ice on Phase Partitioning of Arctic Mixed-Phase Clouds with NCAR CAM5. Journal of Geophysical Research: Atmospheres, 124(23), 13071–13090. https://doi.org/10.1029/2019JD030502

Zhang, M., Xie, S., Liu, X., Lin, W., Zhang, K., Ma, H.-Y., et al. (2020). Toward understanding the simulated phase partitioning of arctic single-layer mixed-phase clouds in E3SM. Earth and Space Science, 7, e2020EA001125. https://doi.org/10.1029/2020EA001125

Zhang, M., Xie, S., Liu, X., Zhang, D., Lin, W., Zhang, K., et al. (2023). Evaluating EAMv2 Simulated High Latitude Clouds Using ARM Measurements in the Northern and Southern Hemispheres. Journal of Geophysical Research: Atmospheres, 128(15), e2022JD038364. https://doi.org/10.1029/2022JD038364

Zhang, Y., Xie, S., Lin, W., Klein, S. A., Zelinka, M., Ma, P.-L., et al. (2019). Evaluation of clouds in version 1 of the E3SM atmosphere model with satellite simulators. Journal of Advances in Modeling Earth Systems, 11, 1253–1268. https://doi.org/10.1029/2018MS001562

Zhao, L., Wang, Y., Zhao, C., Dong, X., & Yung, Y. L. (2022). Compensating Errors in Cloud Radiative and Physical Properties over the Southern Ocean in the CMIP6 Climate Models. Advances in Atmospheric Sciences, 39(12). https://doi.org/10.1007/s00376-022-2036-z

Zhao, X., Liu, X., Burrows, S., DeMott, P. J., Diao, M., McFarquhar, G. M., et al. (2023). Important Ice Processes Are Missed by the Community Earth System Model in Southern Ocean Mixed-Phase Clouds: Bridging SOCRATES Observations to Model Developments. Journal of Geophysical Research: Atmospheres, 128(4). https://doi.org/10.1029/2022JD037513

Table 1. Comparisons of the average cloud fraction, LWP, and net surface SW and LW radiation between Q2 & Q3 and Q1 & Q4 for observations and simulations in MICRE and AWARE.

Variables	MICRE			AWARE		
	Q2 & 3	Q1 & 4	|T|	Q2 & 3	Q1 & 4	|T|
CF OBS	0.8931	0.8986	0.45 *	0.7553	0.6542	*7.46*
CF CAM6	0.9408	0.9520	1.61	0.7735	0.6544	*8.17*
CF EAMv1	0.9646	0.9501	*2.43*	0.7053	0.5226	*12.07*
dCF CAM6	0.0169	0.0383	1.27	0.0349	-0.0367	*4.61*
dCF EAMv1	0.1246	0.1057	1.39	-0.0722	-0.1359	*4.68*
LWP OBS (kg/m²)	0.0844	0.0772	1.80	0.0214	0.0149	*4.00*
LWP CAM6 (kg/m²)	0.1364	0.1521	2.69	0.0252	0.0205	1.60
LWP EAMv1 (kg/m²)	0.0998	0.1292	*8.02*	0.0234	0.0060	*11.42*
dLWP CAM6 (kg/m²)	0.0594	0.0705	*1.66*	0.0032	0.0031	0.02
dLWP EAMv1 (kg/m²)	0.0247	0.0507	*5.11*	-0.0043	-0.0116	*4.53*
IWP OBS (kg/m²)	0.0687	0.0810	*1.99*	0.0368	0.0379	0.29
IWP CAM6 (kg/m²)	0.0096	0.0114	*3.06*	0.0024	0.0020	*2.67*
IWP EAMv1 (kg/m²)	0.0124	0.0096	*4.37*	0.0026	0.0021	*3.74*
dIWP CAM6 (kg/m²)	-0.0574	-0.0562	0.20	-0.0271	-0.0364	*2.89*
dIWP EAMv1 (kg/m²)	-0.0475	-0.0632	*3.03*	-0.0378	-0.0311	*2.02*
SW OBS (W/m²)	100.6071	82.3412	*3.31*	109.0580	92.6947	*3.18*
SW CAM6 (W/m²)	85.5737	85.7278	0.03	117.5711	93.7900	*2.27*
SW EAMv1 (W/m²)	76.1329	86.1451	1.95	116.6847	104.3017	*2.33*
dSW CAM6 (W/m²)	4.0713	-4.1469	*2.54*	11.6501	13.1566	0.59
dSW EAMv1 (W/m²)	1.8820	1.4762	0.14	12.0925	11.8888	0.12
LW OBS (W/m²)	-21.7609	-14.9637	*5.59*	-56.5636	-60.6723	*2.90*
LW CAM6 (W/m²)	-33.5267	-17.8421	*15.73*	-50.8223	-49.6846	*1.25*
LW EAMv1 (W/m²)	-31.8418	-17.0154	*18.12*	-51.8221	-57.7519	*7.05*
dLW CAM6 (W/m²)	-11.6276	-0.8038	*9.08*	8.7343	8.9403	0.15
dLW EAMv1 (W/m²)	-10.9050	0.3734	*10.73*	3.1776	1.7216	1.40

*Statistically significant differences between the two regimes are highlighted in *italics*, which is defined as $|T| > t_{0.95}$. Here $t_{0.95} = 1.96$, calculated using the two-tail t-test at the 95% confidence interval. Underlined |T| values indicate higher values in Q1 and Q4 (i.e., the warm frontal region in eastern sector) and lower values in Q2 and Q3 (i.e., the cold post-frontal western sector).

Table 2. Similar to Table 1, but for comparisons between two regimes of ω_{500}’ > 0 and ω_{500}’ ≤ 0.

Variables	MICRE			AWARE		
	ω_{500}’ > 0	ω_{500}’ ≤ 0	|T|	ω_{500}’ > 0	ω_{500}’ ≤ 0	|T|
CF OBS	0.8915	0.904	1.06 *	0.6138	0.8205	*14.70*
CF CAM6	0.9352	0.954	*2.73*	0.7343	0.6861	*3.21*
CF EAMv1	0.9259	0.9834	*9.51*	0.6023	0.5757	1.57
dCF CAM6	-0.0022	0.0387	*2.55*	0.0313	-0.0429	*4.69*
dCF EAMv1	0.1198	0.1025	1.36	-0.1007	-0.1534	*3.24*
LWP OBS (kg/m²)	0.0966	0.1015	0.77	0.014	0.025	*4.00*
LWP CAM6 (kg/m²)	0.1418	0.147	0.93	0.0224	0.0232	0.27
LWP EAMv1 (kg/m²)	0.0836	0.1477	*19.2*	0.0092	0.0097	0.40
dLWP CAM6 (kg/m²)	0.0689	0.0595	1.43	0.00007	0.0075	*2.07*
dLWP EAMv1 (kg/m²)	0.011	0.0665	*11.43*	-0.013	-0.0095	*2.00*
IWP OBS (kg/m²)	0.088	0.0776	1.64	0.0176	0.0628	*11.89*
IWP CAM6 (kg/m²)	0.0088	0.0121	*6.43*	0.0025	0.0018	*4.39*
IWP EAMv1 (kg/m²)	0.0099	0.0114	*2.31*	0.0021	0.0017	*2.81*
dIWP CAM6 (kg/m²)	-0.0491	-0.0698	*3.64*	-0.0351	-0.027	*2.55*
dIWP EAMv1 (kg/m²)	-0.018	-0.1101	*16.8*	-0.033	-0.0253	*2.48*
SW OBS (W/m²)	94.4634	97.7646	0.59	94.4529	74.4002	*4.17*
SW CAM6 (W/m²)	92.1424	87.2763	*0.85*	105.048	106.0821	0.08
SW EAMv1 (W/m²)	96.3371	78.6174	*3.36*	106.5067	117.6624	1.89
dSW CAM6 (W/m²)	-1.8353	1.5304	1.07	10.8144	3.8436	0.64
dSW EAMv1 (W/m²)	1.4223	2.7548	0.46	12.2731	15.4239	1.76
LW OBS (W/m²)	-22.5687	-13.6375	*7.45*	-63.1567	-46.0194	*11.74*
LW CAM6 (W/m²)	-30.6093	-19.5213	*11.24*	-48.0286	-53.1619	*5.57*
LW EAMv1 (W/m²)	-32.5702	-14.8369	*22.39*	-56.8248	-60.5154	*4.32*
dLW CAM6 (W/m²)	-6.3109	-5.4308	0.74	8.7107	9.2576	0.41
dLW EAMv1 (W/m²)	-3.6199	-6.0637	*2.34*	-0.0562	2.0066	1.71

*Similar to Table 1, |T| > $t_{0.95}$ indicates statistically significant differences between two sectors and are marked in *italics*. Underline indicates higher values in the region of ω_{500}’ ≤ 0 (i.e., the warm frontal region with ascent motion) than the regions of ω_{500}’ > 0 (i.e., the cold post-frontal region with descent motion).

Table 3. Linear regression slope and r^2 values for net surface SW and LW radiation binned by various ranges of observed CF, LWP, and IWP, and model biases of dCF, dLWP, and dIWP.

Variables	Bin ranges	MICRE				AWARE			
		CAM6 SW	EAMv1 SW	CAM6 LW	EAMv1 LW	CAM6 SW	EAMv1 SW	CAM6 LW	EAMv1 LW
CF	(0 to 0.1)	**0.931** (0.844)	0.833 (0.842)	**0.469** (0.377)	**0.437** (0.456)	**0.972** (0.846)	**1.007** (0.961)	**0.278** (0.286)	**0.295** (0.521)
	(0.1 to 0.9)	0.890 (0.694)	0.899 (0.842)	0.366 (0.204)	0.393 (0.276)	0.913 (0.797)	0.978 (0.932)	0.246 (0.154)	0.272 (0.288)
	(0.9 to 1)	0.915 (0.814)	**0.985** (0.765)	0.346 (0.180)	0.382 (0.245)	0.918 (0.768)	1.024 (0.882)	0.146 (0.033)	0.129 (0.041)
LWP (kg m^{-2})	(0 to 0.025)	0.875 (0.746)	0.848 (0.792)	**0.382** (0.202)	0.401 (0.291)	0.972 (0.832)	**1.013** (0.947)	**0.333** (0.290)	**0.391** (0.442)
	(0.025 to 0.05)	**0.949** (0.762)	**0.984** (0.816)	0.374 (0.197)	**0.419** (0.283)	**1.009** (0.652)	1.146 (0.796)	0.114 (0.014)	0.271 (0.051)
	(> 0.05)	0.896 (0.659)	0.946 (0.732)	0.321 (0.188)	0.348 (0.273)	1.134 (0.603)	1.279 (0.725)	0.100 (0.003)	0.069 (0.005)
IWP (kg m^{-2})	(0 to 0.1)	**0.909** (0.725)	**0.844** (0.688)	0.427 (0.292)	0.317 (0.259)	0.941 (0.785)	**1.002** (0.905)	**0.250** (0.160)	0.289 (0.269)
	(0.1 to 0.2)	1.253 (0.746)	1.159 (0.685)	0.527 (0.343)	0.488 (0.362)	**1.009** (0.716)	1.051 (0.827)	0.009 (0.000)	0.148 (0.022)
	(> 0.2)	1.494 (0.451)	1.338 (0.722)	**0.711** (0.198)	**0.589** (0.443)	1.464 (0.810)	1.335 (0.873)	0.099 (0.007)	**0.385** (0.117)
dCF	(-0.5 to 0.5)	0.853 (0.718)	**0.893** (0.765)	0.292 (0.162)	0.316 (0.224)	**0.957** (0.787)	**1.008** (0.904)	**0.324** (0.248)	**0.400** (0.380)
	(0.5 to 0.9)	**0.872** (0.688)	0.839 (0.779)	**0.396** (0.208)	**0.325** (0.193)	0.804 (0.816)	0.929 (0.893)	0.159 (0.057)	0.249 (0.199)
	(-0.5 to -0.9)	1.135 (0.950)	1.164 (0.725)	0.076 (0.033)	0.031 (0.009)	1.059 (0.773)	1.062 (0.903)	0.182 (0.307)	0.251 (0.432)
dLWP (kg m^{-2})	(-0.1 to 0.1)	**1.074** (0.862)	**0.952** (0.823)	**0.388** (0.224)	0.399 (0.324)	**1.001** (0.854)	**1.023** (0.962)	**0.322** (0.455)	**0.393** (0.557)
	(0.1 to 0.5)	0.814 (0.764)	0.797 (0.816)	0.209 (0.140)	0.191 (0.147)	0.769 (0.856)	0.838 (0.903)	0.106 (0.136)	0.207 (0.538)
	(-0.1 to -0.5)	1.097 (0.836)	1.106 (0.854)	0.308 (0.165)	**0.401** (0.293)	1.253 (0.803)	1.295 (0.894)	0.293 (0.205)	0.294 (0.151)
dIWP (kg m^{-2})	(0 – 0.1)	**0.909** (0.787)	0.744 (0.728)	0.383 (0.297)	0.281 (0.251)	0.937 (0.818)	0.946 (0.929)	0.222 (0.139)	0.298 (0.273)
	(-0.1 to 0)	1.212 (0.626)	**1.209** (0.709)	**0.580** (0.219)	0.510 (0.403)	**0.973** (0.758)	**1.043** (0.884)	**0.296** (0.178)	**0.355** (0.284)
	(-0.5 to -0.1)	1.1682 (0.929)	1.798 (0.904)	0.574 (0.142)	**0.549** (0.242)	1.367 (0.832)	1.684 (0.777)	0.013 (0.000)	0.246 (0.037)

*The two values in each textbox denote linear regression slope values and coefficients of determination, i.e., b (r^2). The slope values closest to 1 in each category are highlighted in **bold**.

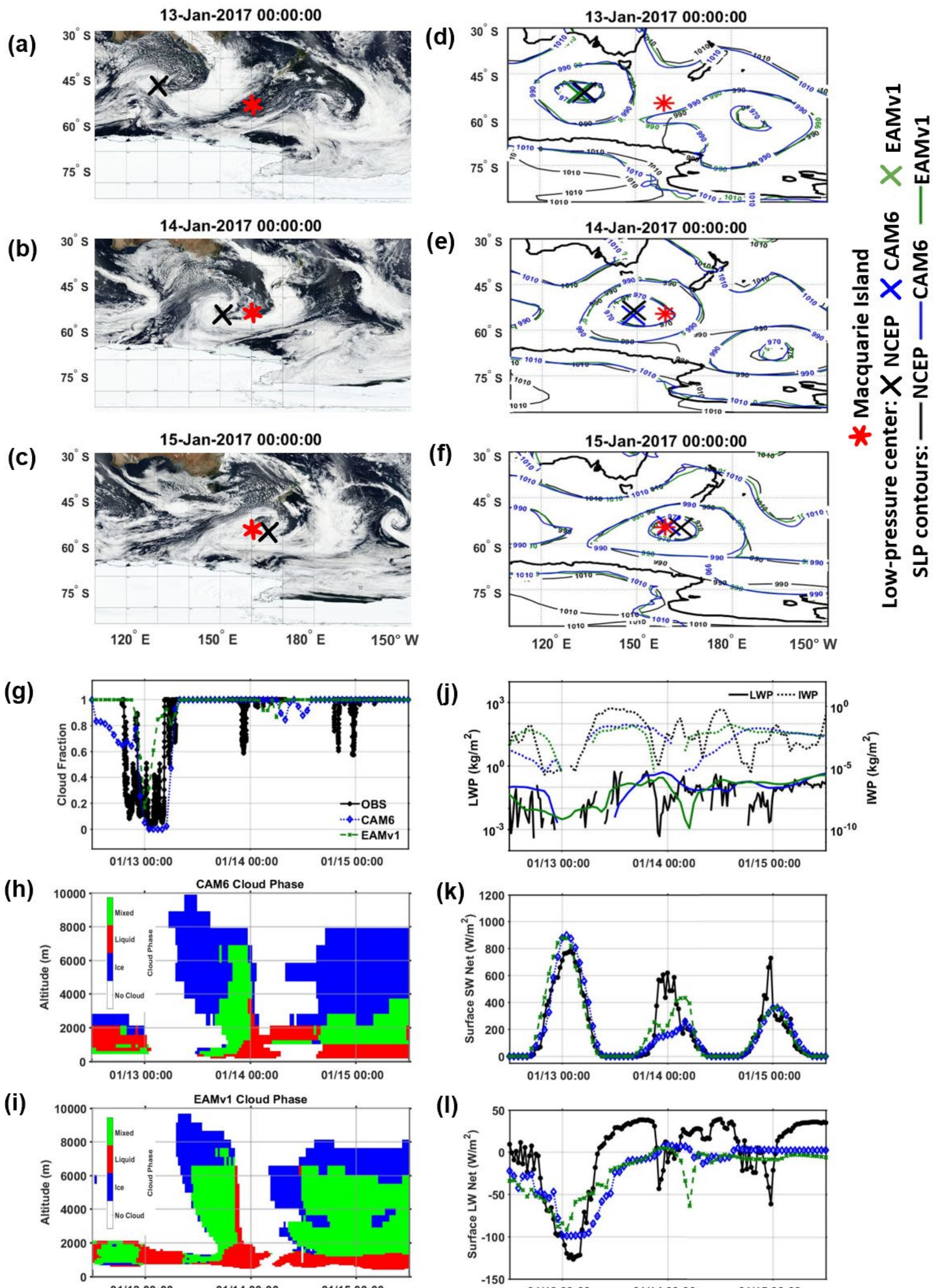

Figure 1. A case study of MICRE campaign from 12 UTC, January 12, 2017 to 12 UTC, January 15, 2017. (a) Observed and simulated cloud fraction. (b, c) Cloud phase for CAM6 and EAMv1, respectively. (d-f) LWP, IWP, net surface SW and LW, respectively. (g-i) GOES-16 satellite images (clean infrared 10.3 µm, band 13). (j-l) Sea level pressure contour maps in units of hectopascal based on NCEP reanalysis in black, CAM6 in blue and EAMv1 in green contours. Cross markers in g-l illustrate the position of low-pressure centers for NCEP (red), CAM6 (blue) and EAMv1 (green).

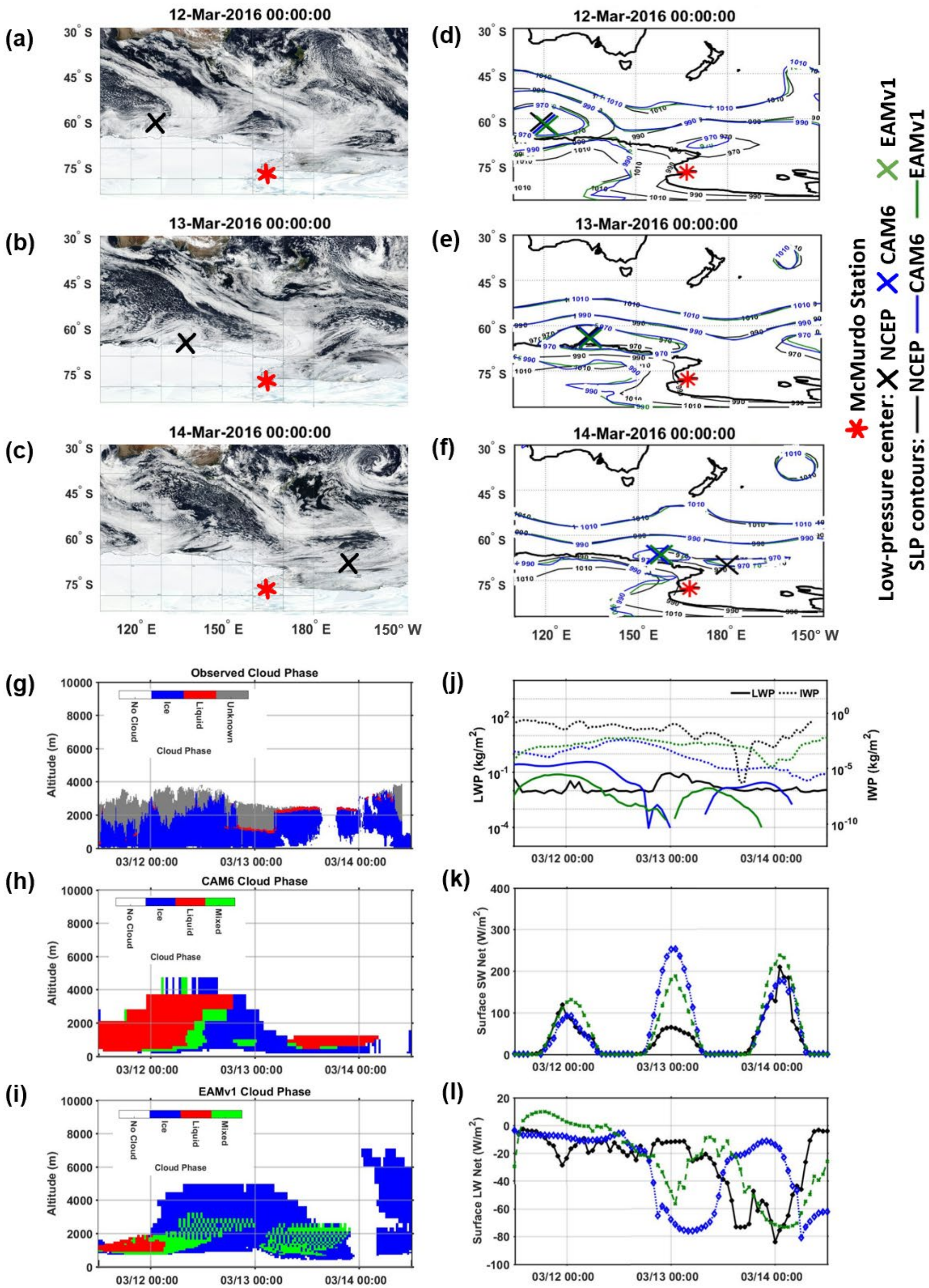

Figure 2. Similar to Figure 1, but for a case study of AWARE campaign from 12 UTC, March 11, 2016 to 12 UTC, March 14, 2016. Different from Figure 1a, Figure 2a illustrates observed cloud phase.

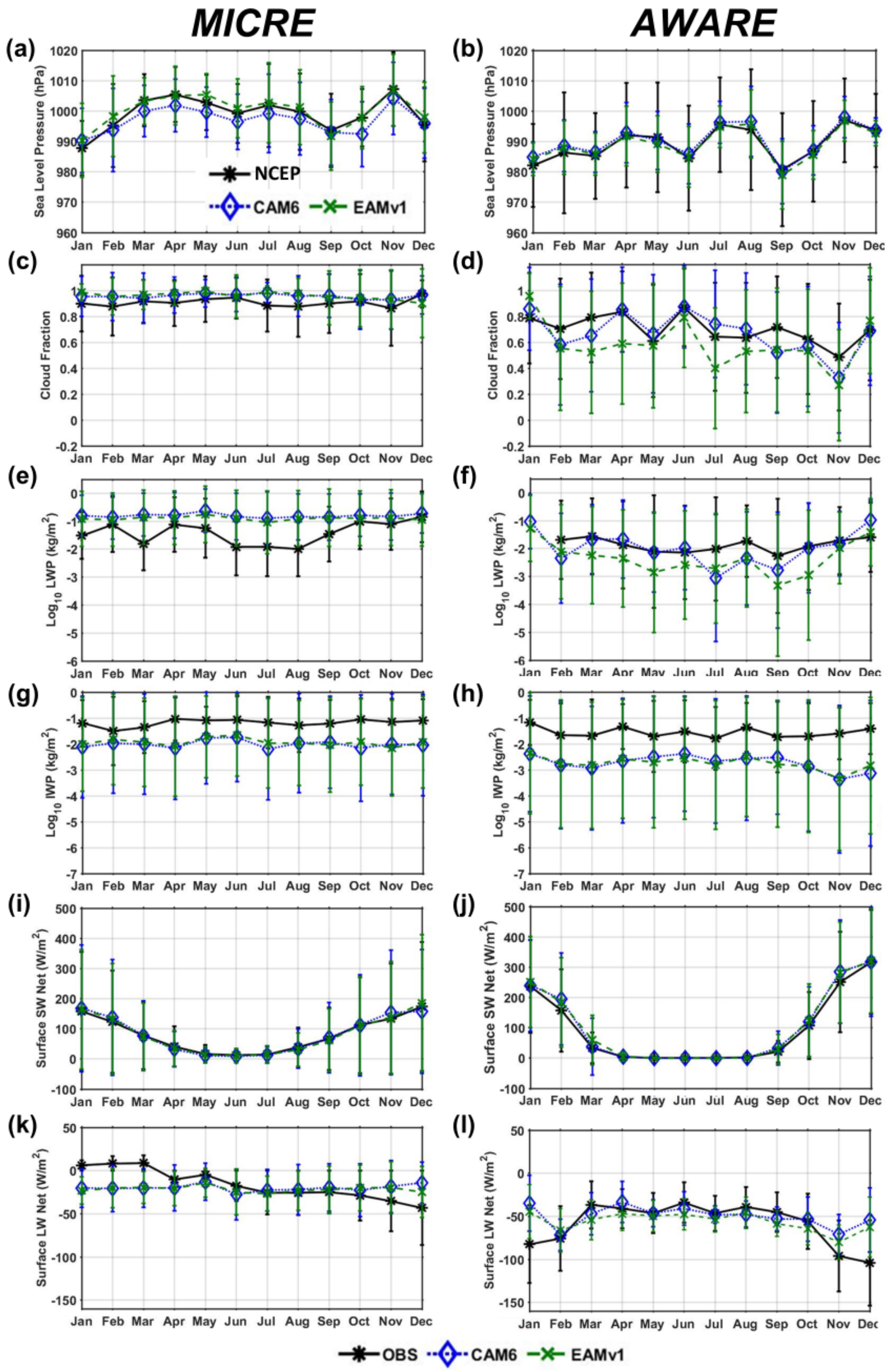

Figure 3. Monthly averages of (a, b) sea level pressure, (c, d) cloud fraction, (e, f) LWP, (g, h) IWP, (i, j) net surface SW and (k, l) LW radiation from observations and simulations. Black lines in all panels stand for ground-based observations, except for panel (a) which shows NCEP data in black line.

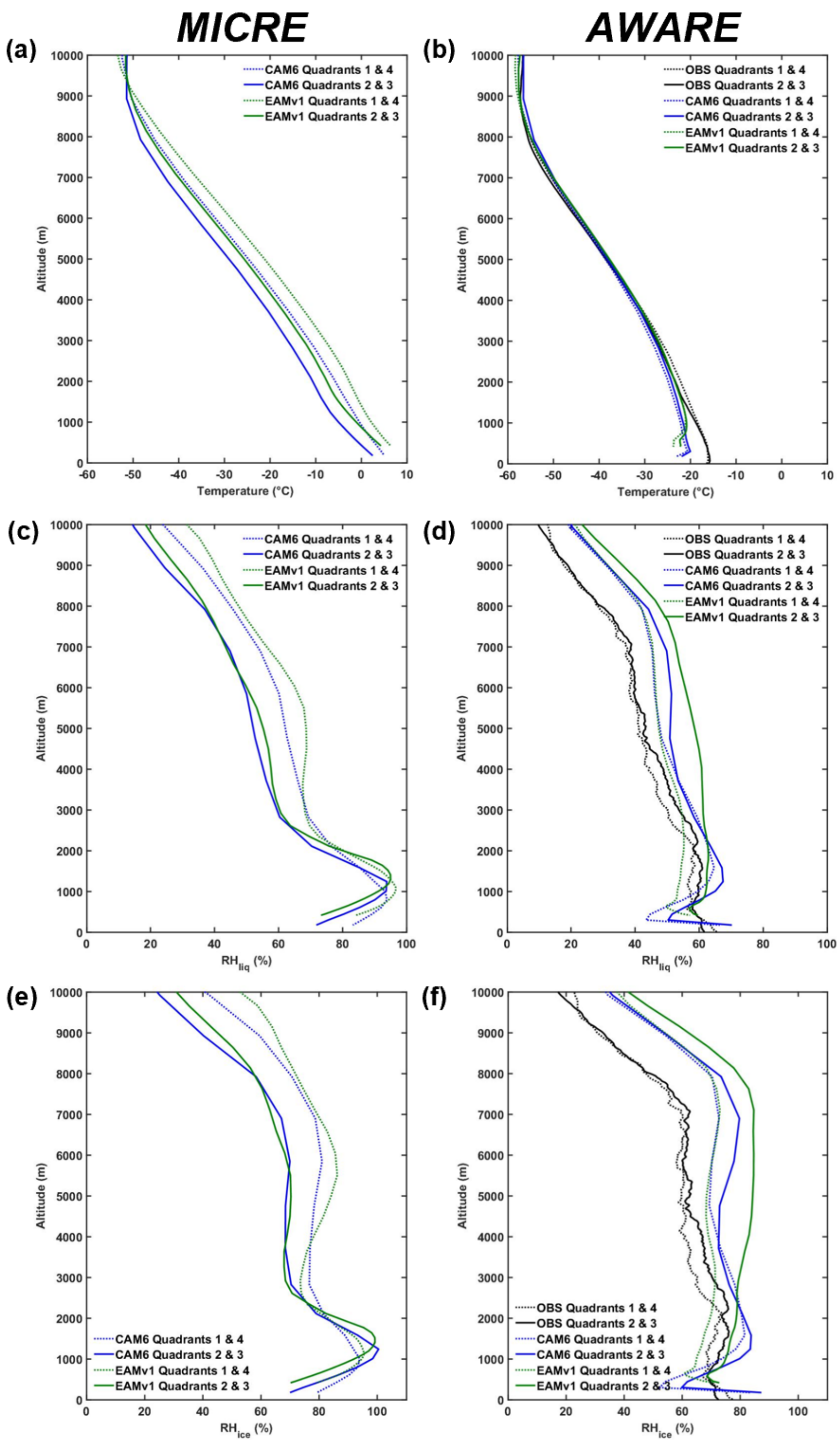

Figure 4. Vertical profiles of temperature, RHice, and RHliq, separated by the eastern (Q1 & Q4) and western (Q2 & Q3) sectors, based on observations and simulations.

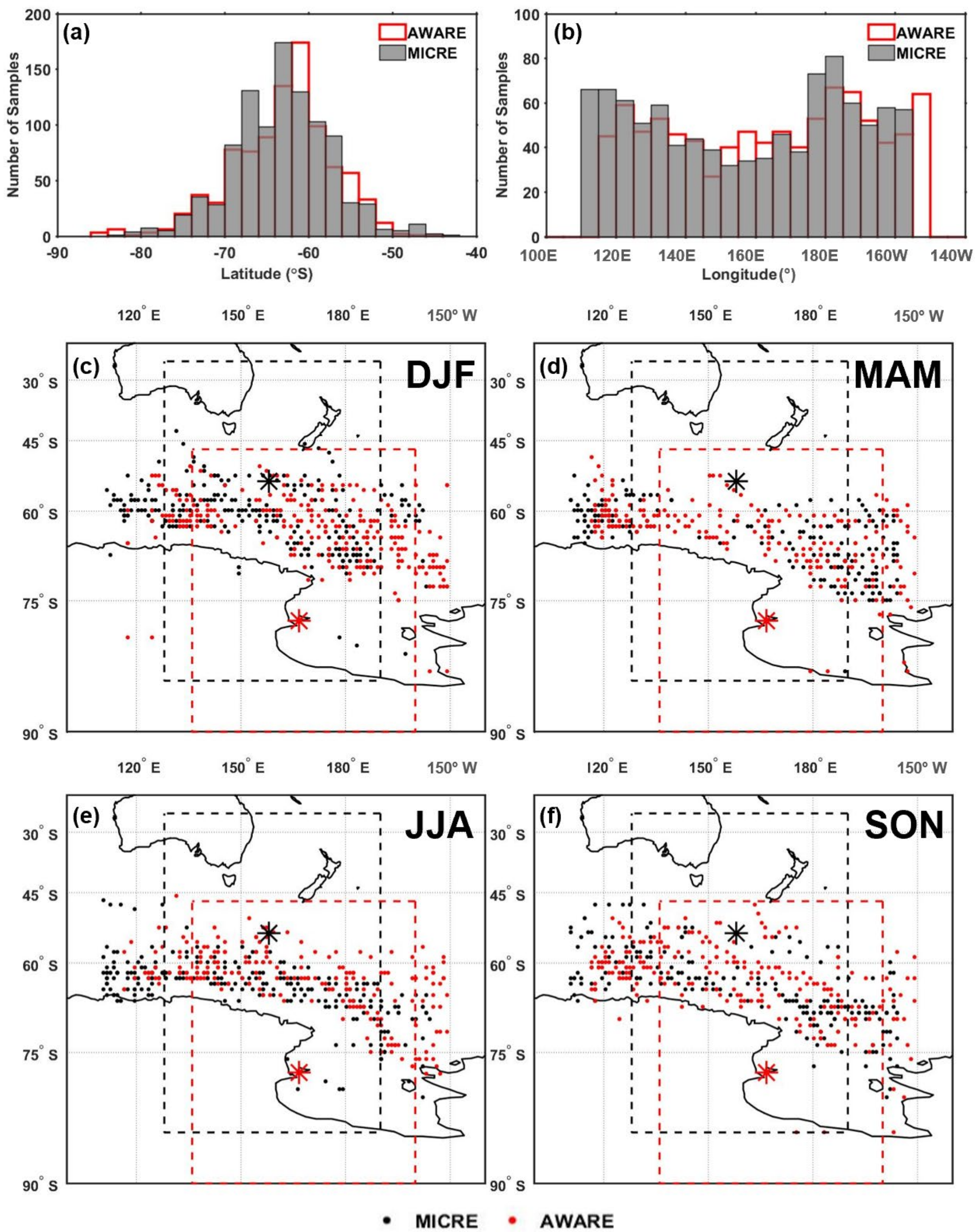

Figure 5. (a) Latitudinal and (b) longitudinal distributions of extratropical cyclones surrounding each station, using 6-hourly frequency of NCEP data. (c-f) Locations of low-pressure centers of extratropical cyclones in four seasons. The black and red boxes in (c) – (f) denote the ±30 degrees latitude and ±30 degrees longitude box surrounding MICRE and AWARE stations, respectively. These boxes are used to identify low-pressure centers, which are defined as the sea level pressure minima within that box.

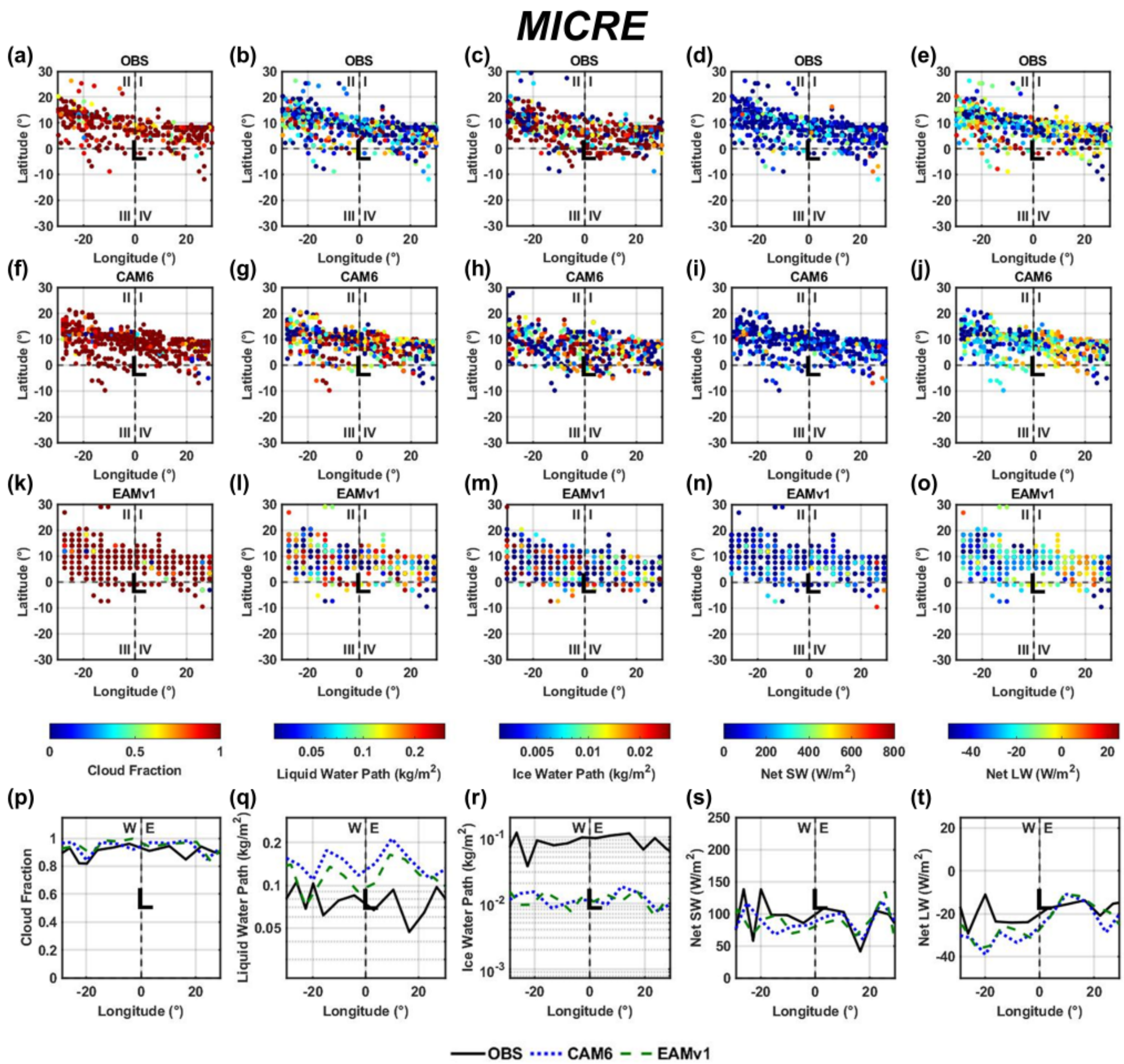

Figure 6. Distributions of cloud and radiative properties in a relative coordinate with respect to low-pressure centers of extratropical cyclones for the MICRE campaign. Columns 1 to 5 represent cloud fraction, LWP, IWP, net SW and LW, respectively. The first three rows represent observations, CAM6 and EAMv1 simulations, respectively. The last row represents the average values in each longitudinal bin. The "L" marker located at (0, 0) indicates the low-pressure center. Four quadrants, Q1–Q4, are labeled as I, II, III and IV, respectively, indicating ground stations located at the northeast, northwest, southwest, and southeast side relative to the low-pressure centers. Two sectors (eastern or western) are labelled in the bottom row.

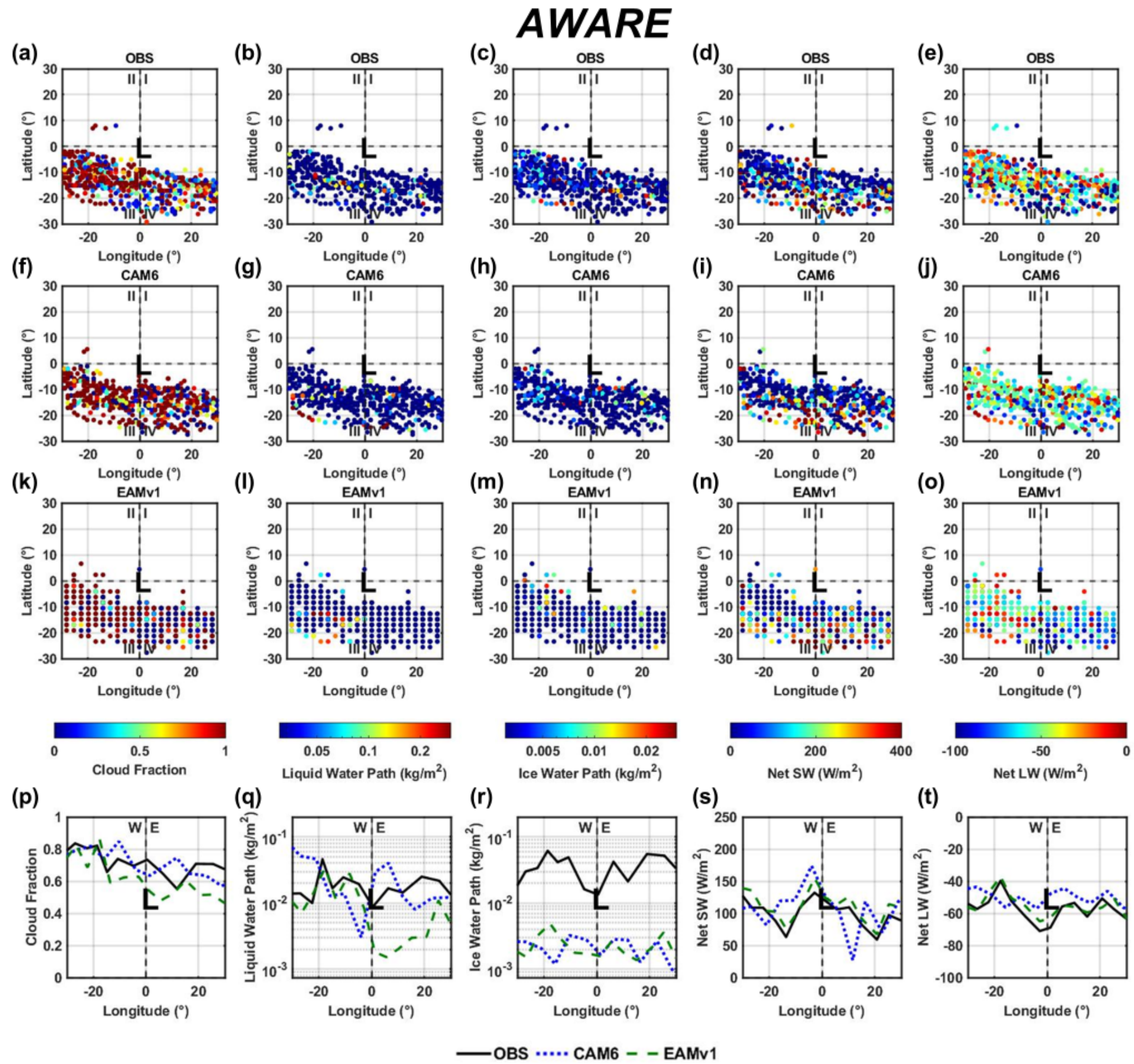

Figure 7. Similar to Figure 6, except for the AWARE campaign.

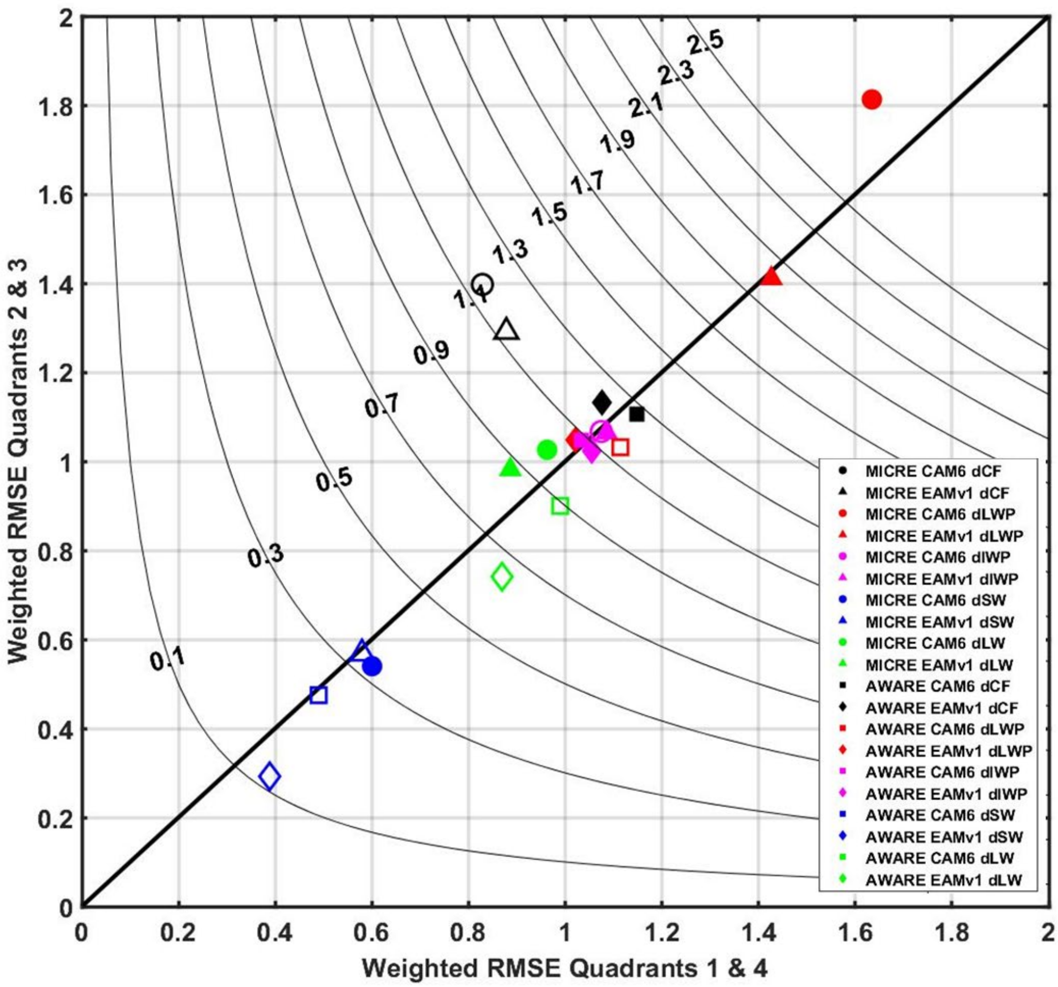

Figure 8. Weighted RMSE calculated for CAM6 and EAMv1 simulations, separately shown for Q2 & Q3 (western sector) and Q1 & Q4 (eastern sector) in ordinate and abscissa, respectively. Black solid line indicates 1:1 line. Thin black curves indicate the multiplications of the weighted RMSE values in both sectors. Filled markers indicate RMSE values with statistically significant differences between the two sectors, that is, their differences pass the t-test with 95% confidence interval, while the unfilled markers indicate no statistically significant differences.

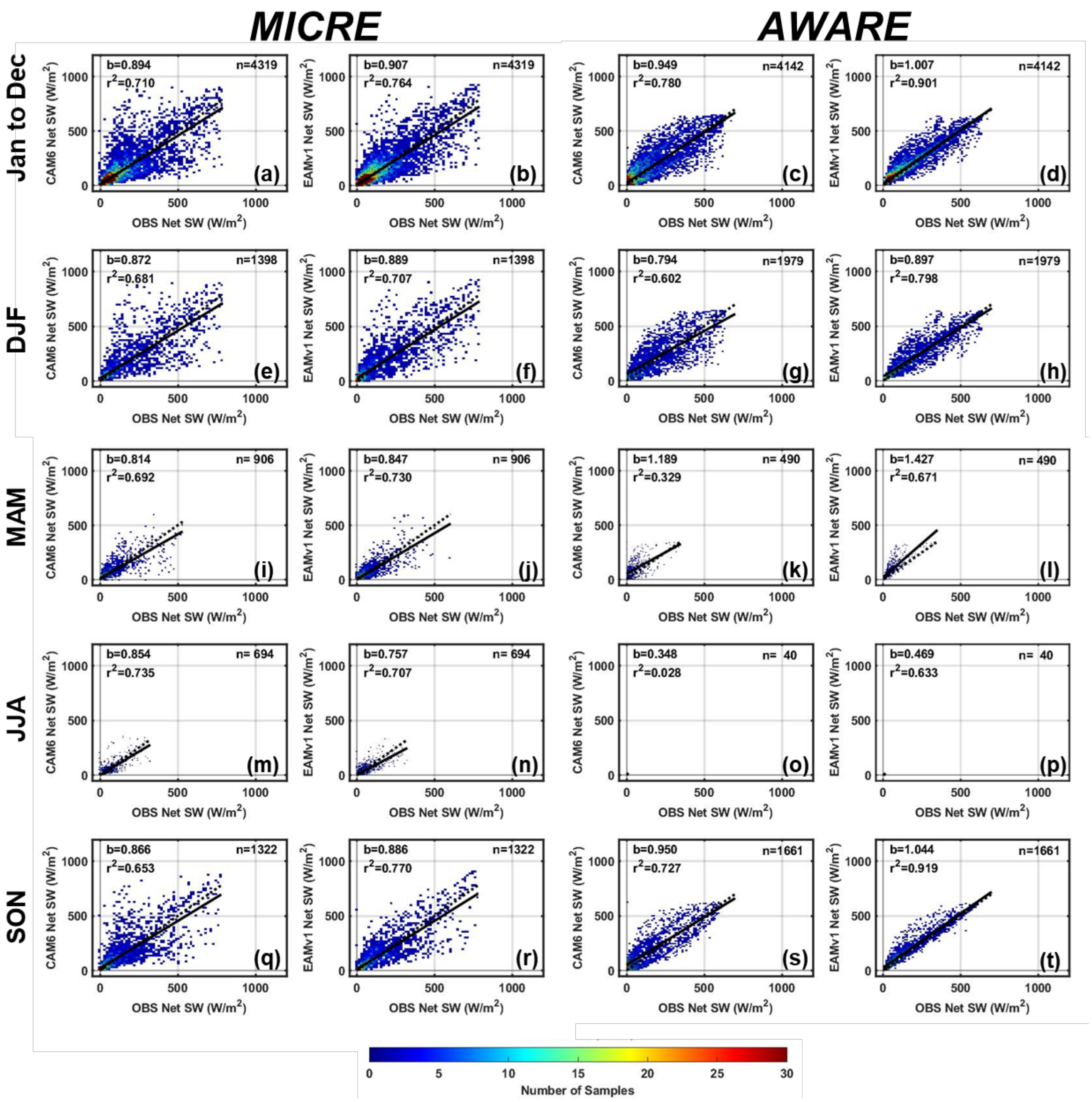

Figure 9. Seasonal variations of net surface SW radiation compared between observations and simulations. Data are gridded and the color code shows the number of samples in each grid. Row 1 is for all seasons, while rows 2 – 5 are for different seasons (i.e., DJF, MAM, JJA and SON). Black lines show linear regressions. The slope, coefficient of determination, and number of counts are denoted by b, r^2 and n, respectively.

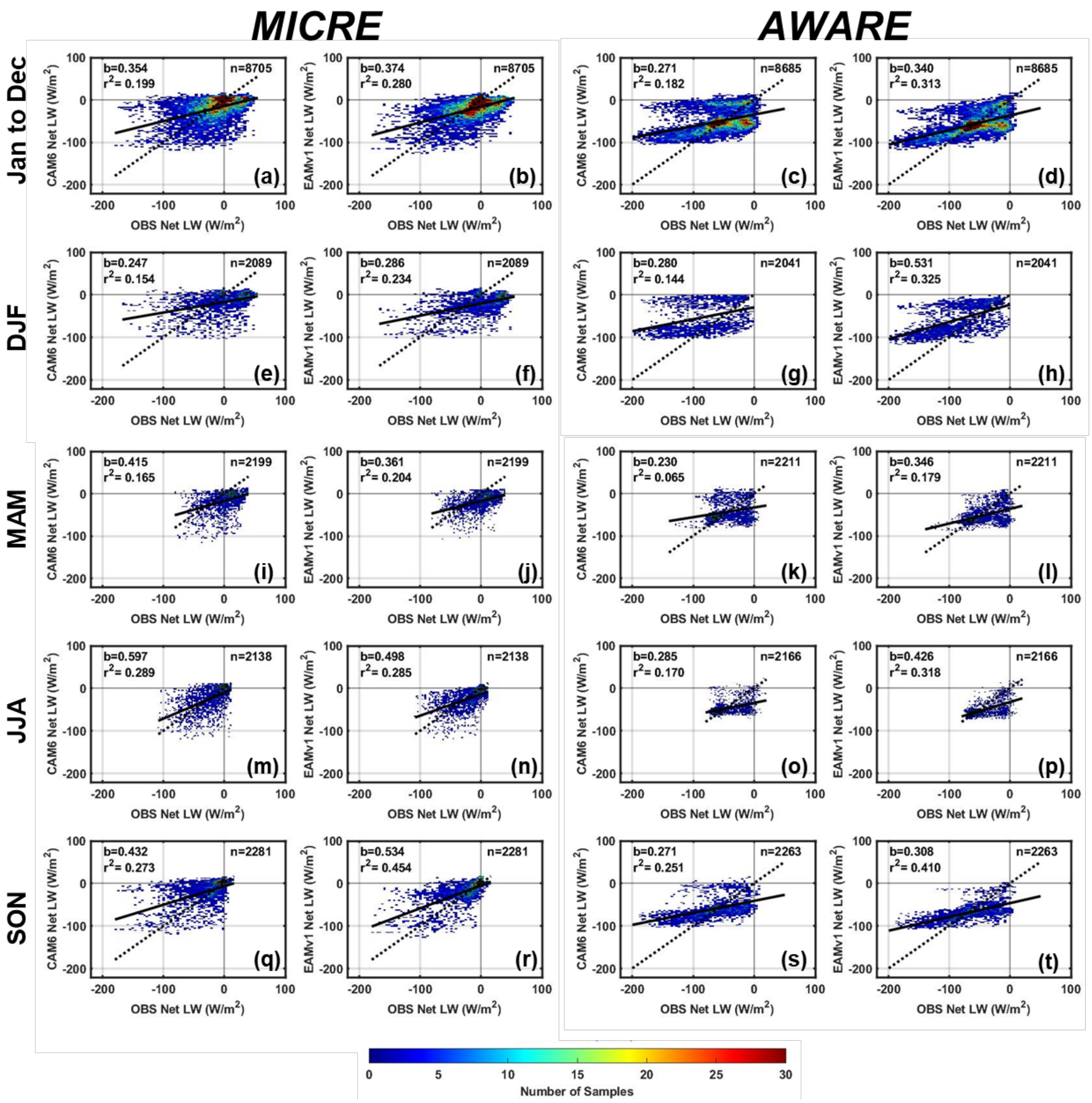

Figure 10. Same as Figure 9, except for analysis of net surface LW radiation.

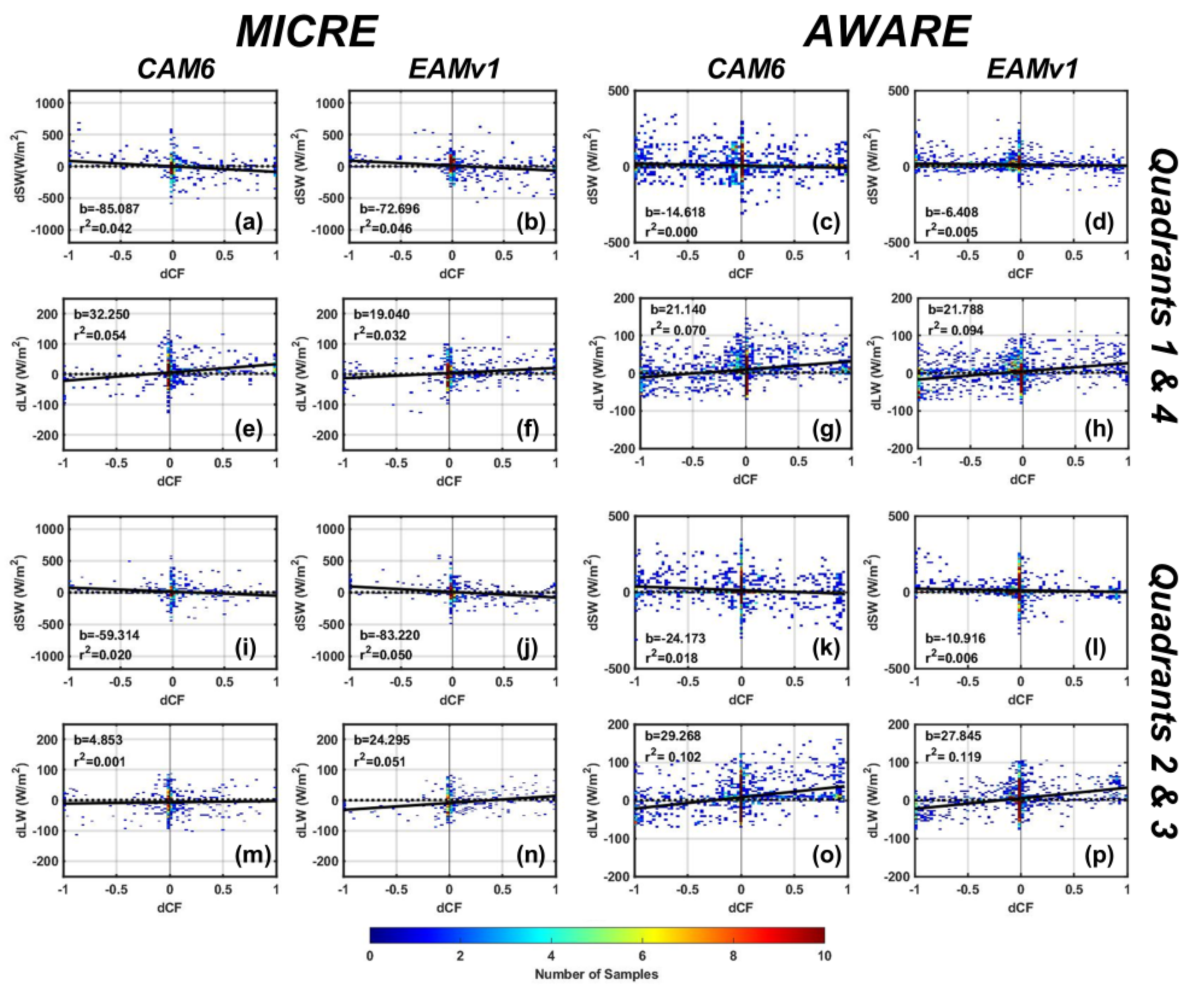

Figure 11. Correlations between model biases of net surface radiation (dSW and dLW) and cloud fraction biases (dCF) shown in the (a-h) eastern and (i-p) western sectors. Rows 1 and 3 show dSW, while rows 2 and 4 show dLW.

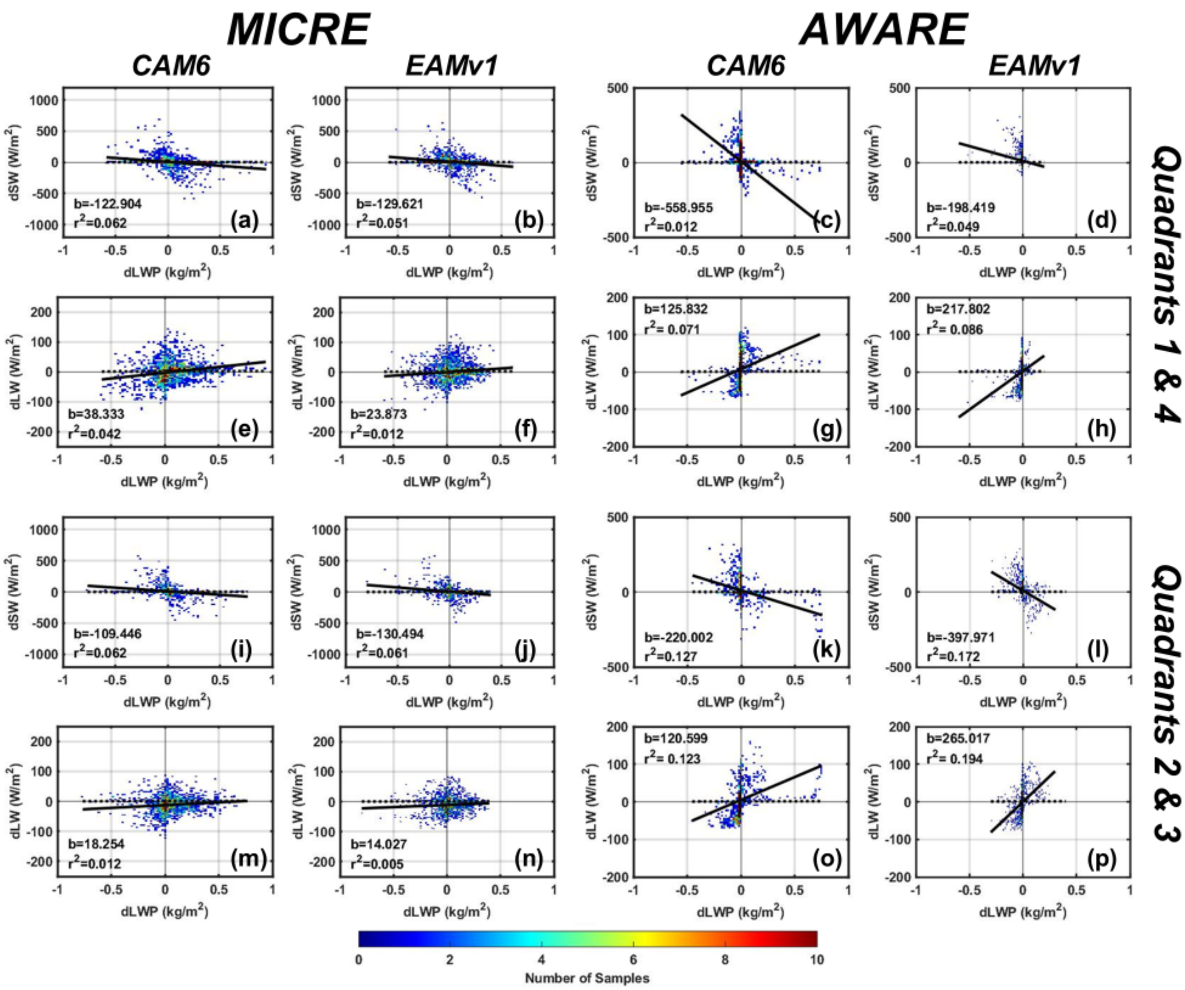

1291

1292 **Figure 12.** Similar to Figure 11, except for correlations between radiation biases and dLWP.

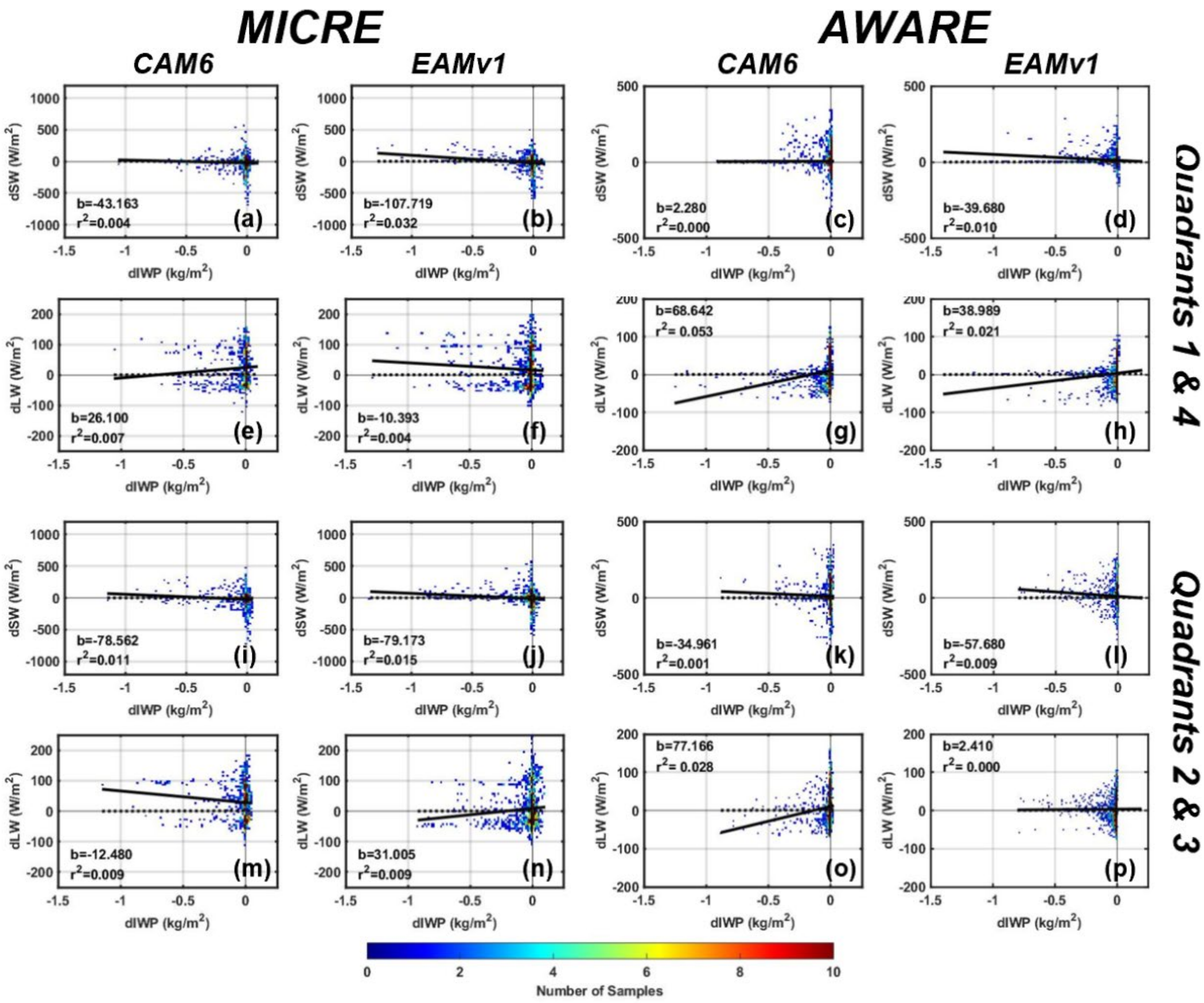

Figure 13. Similar to Figure 11, except for correlations between radiation biases and dIWP.